3D Additive Manufacturing

WAAM Martensitic Stainless Steel: Process Optimization & Resulting Weld Geometrical Characterization

Vignesh Venkata Subramanian

Process Parameters
Microstructure &
Microhardness

TU Delft

3D Additive Manufacturing

WAAM Martensitic Stainless Steel: Process Optimization & Resulting Weld Geometrical Characterization

by

Vignesh Venkata Subramanian

to obtain the degree of Master of Science
at the Delft University of Technology,
to be defended publicly on December 20, 2017.

Student number:	4507002	
Project duration:	June 1, 2017 – December 20, 2017	
Thesis committee:	Ass. Prof. Dr. Ir. M. Hermans,	TU Delft, Chair
	Dr. Wei Ya,	University of Twente, Ramlab
	Ir. K. Goulas,	TU Delft, supervisor
	Prof. Dr. Ir. Roumen H. Petrov,	Universiteit Ghent

This thesis is confidential and cannot be made public until December 20, 2017

TU Delft

RAMLAB
metal parts on demand

Abstract

Wire Arc Additive Manufacturing (WAAM), one of the Additive Manufacturing (AM) deposition methods which employs the basic principles of Gas Metal Arc Welding (GMAW) welding technique was used to show that it is possible to build moulds for ceramic products using AISI 420 stainless steel due to its characteristics such as corrosion resistance, machinability, hardness and dimensional stability. The WAAM process also is efficient in terms of its deposition rate, reduced material wastage and high surface quality.

To investigate the feasibility of AM of AISI 420 stainless steel using WAAM, Response Surface Methodology (RSM - a predictive technique) was used to navigate within the input parameter range for process optimization. Bead-on-plate welding experiments were performed with a MIG welding robot on a structural steel (S355J2) as the substrate. In the tested range according to RSM analyses, the optimum weld condition was 261 A (Current), 29 V (Volts) and 0.59 m/min S (Travel Speed) with preheating at 200°C. However, this condition was found to be unsuitable for AM due to its low deposition speed, non - uniform building surface morphology and inter-run porosities when overlapping welds were deposited. Further analyses on the metallurgy of the WAAM AISI 420 stainless steel through Scanning Electron Microscope (SEM) revealed that the weld metal consisted of a martensite matrix and δ-ferrite at the grain boundaries. The Vickers Hardness of the weld metal was 514HV.

To achieve WAAM feasibility using AISI 420 stainless steel, modified RSM method was performed by expanding the input parameters and visually inspecting the bead for its shape, size and quality. The experiment adopted was called the Ramping Procedure wherein a single resulting weld bead can represent many input parameter combinations. The optimum condition for the input parameters were identified to be 200 A (Current), 18.5 V (Volts) and 1.00 m/min S (Travel Speed). With the optimal processing conditions, rectangular blocks or walls were modelled and designed in the Autodesk Powermill software and built to evaluate the feasibility of WAAM AISI 420 stainless steel. Samples were built without preheating and no surface defects and cracking were observed. Microstructural and hardness studies were then performed. Results show that the as-welded weld metal consisted of δ-ferrite present in a martensite matrix. The hardness of the weld metal was 623 HV.

The WAAM optimization procedure for AISI 420 stainless steel that has not been explored for AM processes due to its high sensitivity to welding thermal cycles that can lead to cracking. In this study, it has been successfully demonstrated that crack free AISI 420 stainless steel can be deposited with WAAM.

Acknowledgements

I would like to thank **Ass. Prof. Dr. Ir. Marcel Hermans**, TU Delft to introduce me to Ramlab whereby I was able to work on this very interesting research topic.

I would like to convey my heartfelt thanks to **Dr. Wei Ya**, University of Twente and Ramlab to guide and mentor me throughout the entire course of my thesis.

I would like to thank **Ir. Konstantinos Goulas**, TU Delft to supervise and provide me help and answering my questions whenever needed.

I would like to appreciate **Vincent Wegener**, Ramlab for his effort, involvement and keen interest to arrange all the materials needed for my thesis.

Finally, I thank wholeheartedly my family and friends who supported and helped me to successfully complete this thesis.

Contents

1 Introduction to Additive Manufacturing

1.1. Additive Manufacturing

Additive manufacturing (AM) of metals is a term, which refers to the manufacturing technique known to the public as "3D Metal Printing".

AM has been researched for a few decades [1–3], but it was made possible to produce certain components successfully with this method very recently. Currently, small plastic parts can be printed using a portable printer at home up to large metal components such as a ship's propeller in an industrial framework.

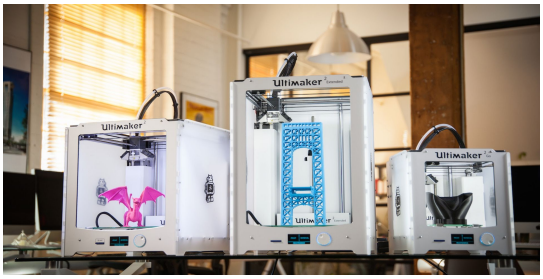

(a) Portable Ultimaker 3D Printer

(b) Ship's Propeller, Ramlab

Figure 1.1: Small to large 3D printed objects

Even though it has been shown that it is possible to build large - scale objects through AM [4], numerous questions remain to be answered. It is of interest for materials scientists and engineers to explore the potentials of different metals and alloys for AM, and which of these could possibly replace the conventional methods of manufacturing such as *casting, forging and milling* as the advantages offered by AM [1]. 3D AM apart from being a fancy term, has advantages over conventional manufacturing processes. One of the main noticeable facts is that the material wastage is drastically reduced, resulting in less environmental impact and suitable for sustainable development. Another advantage of AM is to overcome the machining constraints such as making square holes for example *Figure 1.2 (a)*. Imagine the time and complexity one needs to face just to make a unique tool for that purpose. All these can be easily solved with less time and by using simpler methods, such as AM.

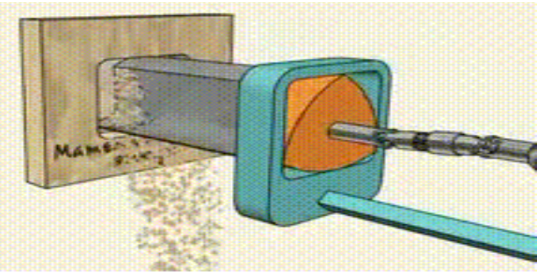

(a) Making a square hole

(b) Complex hollow parts

Figure 1.2: Simplicity of AM

For AM to supplement or replace these conventional methods, a brief comparison is made between them on their specific tasks [5]:

1. Rapid Prototype Production

   With regards to AM, it does not require any kind of tooling to begin with. A part can be 3D printed using a computerised 3D model much faster than conventional methods to plan a production line and setup an assembly process.

2. Waste Optimization (high buy to fly ratio)

   Only the material that is consumed through an extruder of a polymer based 3D printer or a MIG based welding torch robot is used to make the part. In other words, it is resource efficient.

   For example, in sheet metal production, blanks are cut out using a hydraulic press of the required shape leaving the unused part of the sheet metal to waste. The opposite of this happens with AM.

3. Scale of Parts Produced

   Recently, using the Wire Arc Additive Manufacturing (WAAM) technology, large sized prototypes can be made thus breaking the barriers of only 3D printing small parts.

The next section explains about the different types of AM and focuses on Wire Arc Additive Manufacturing (WAAM), which is the focus of the present thesis. *Section 1.3* provides insight about the material used in this research.

1.2. Wire Arc Additive Manufacturing

The main metallic AM methodologies can be summarized as Direct Energy Deposition (DED) [6][7], which includes the following techniques:

1. Selective Laser Sintering (SLS)
2. Selective Laser Melting (SLM)
3. Electron Beam Melting (EBM) and,
4. Wire Arc Additive Manufacturing (WAAM).

The first three deposition methods (SLS, SLM & EBM) use metal in the powder form while WAAM uses a spool of solid welding wire. WAAM is an application of either *Metal - Inert Gas (MIG)* or *Tungsten - Inert Gas (TIG)* Welding technique. But, the deposition efficiency of TIG is low (60%) [8] in terms of the energy input to the work versus the electrical energy consumed by the wire, MIG (~80%) is therefore preferred to be used for AM[9].

Figure 1.3 schematically shows the MIG set up which consists of a shielding gas inlet, a wire feeding unit and a water-cooled torch attached to a robotic arm.

The wire and the shielding gas meet at the welding torch wherein the arc is generated with appropriate combination of the input parameters - *Current, Voltage* and *Travel Speed*.

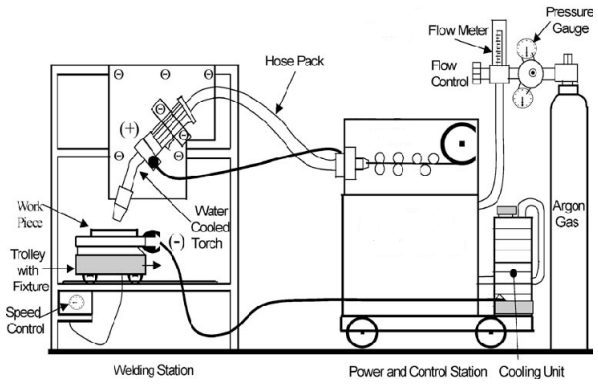

Figure 1.3: MIG Welding Schematic

The advantages of this type of deposition methodology is that parts of any shape size can be made using helpful robot programming software such as *Autodesk Powermill*. Powermill was originally designed to program CNC machines to perform milling operations on as casted products. Recently, a plug-in was developed especially for AM that can read by the robot. The program describes the tool paths the robot should follow to build the parts as designed in the CAD file.

As any other new technologies, WAAM also has some disadvantages. Very complex and intricate parts require more advanced strategies to achieve near - net shape. Some interesting parts contain overhang profiles as shown in *Figure 1.4* which are quite challenging to produce because, they require additional material to physically support the position of the weld pool, so the desired shape can be achieved.

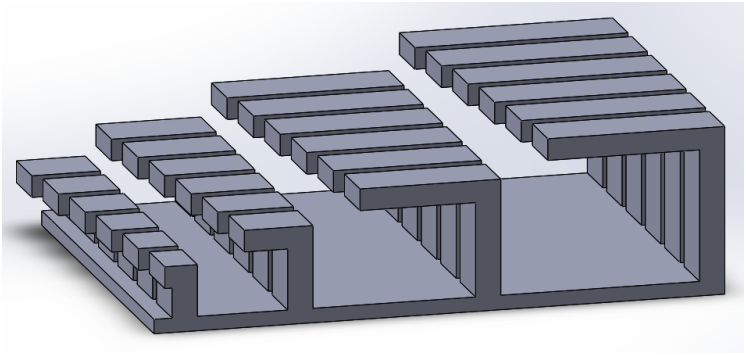

Figure 1.4: Challenging Overhang Profiles [10]

1.3. Stainless Steel - AISI 420

The AISI 420 is a martensitic stainless steel. Martensite is a phase that is formed when the metal is heated to the austenitic phase field and rapidly cooled down. The resulting phase is hard and brittle [11]. Stainless steel means it is resistant to corrosion due to its high chromium content as shown in the *Table 1.1* below. Being hard and corrosion resistant makes AISI 420 suitable for various applications such as moulds for plastic or ceramic components and used to make tools and surgical instruments.

Table 1.1: Chemical Composition of wire used wt.%

Material	C	Cr	Fe	Mn	Mo	Ni	Si
AISI 420	0.38	16	80.77	0.65	1.0	0.8	0.4

Moulds typically require the material to be dimensionally stable, corrosion resistant, hard and machinable [12]. Their hardness is recommended to be in the range of BHN 330, HRC 35 (~332HV) to BHN 500, HRC 50 (~ 505HV) [13]. Moulds that are too soft leads to mould defects such as erosion, sand inclusions, metal penetration and dimensional issues such as over - sized moulds. Moulds that are excessively hard leads to hot tears, hard ram and veining defects [14]. Tool steels and surgical instruments on the other hand require them to be hard, resistant to abrasion and able to remain sharp at elevated temperatures [15] [16].

Villeroy & Boch Wellness, a large German ceramic manufacturing company that makes luxurious bath tubs *Figure 1.5 (a)* and sinks experienced the above said defects in their moulds using AISI 420. They were interested to look into alternative methods to manufacture moulds that are defect free. Therefore, one of the focus in our study is attempting to eliminate those defects using WAAM and produce better quality moulds.

(a) Ceramic Bath Tubs and Sinks [17]

(b) Surgical Instruments [16]

Figure 1.5: Applications of AISI 420

1.4. Research Questions

When attempting to use the AISI 420 material for AM, extensive research must be performed for obtaining successful results. The following are three key points, which are important as a starting point to achieve the successful AM builds.

1. Optimize welding parameters (Current, Voltage and Travel Speed)
2. Porosity and inclusion free weld beads and,
3. Establish a relationship between the obtained microstructure and the welding parameters.

1.5. Structure of the thesis

Further down this report, *Chapter 2 (Literature Review)* - gives a brief overview of the research that has been performed in the past and main outcomes which will be considered in this research. The experimental setup, assumptions, results, discussion and conclusions found in literature are also briefed in this chapter. *Chapter 3 (Experimental Procedure)* - gives a detailed explanation of the steps such as different methodologies, mathematical models, assumptions and other processes that have been used to answer the research questions. *Chapter 4 (Results)* - provides interesting findings and recorded observations from the experiments described in the previous chapter. *Chapter 5 (Discussion)* - explains as to why certain results and observations are found and provide better clarity to the understanding of the research and lastly followed by *Chapter 6 (Conclusion and Recommendations).*

2

Literature Review

The technique employed in this research is Wire Arc Additive Manufacturing (WAAM) which is based on Gas Metal Arc Welding (GMAW). However, from the literature study, it was found that a majority of them have employed laser as heat source instead of Arc for deposition of AISI 420 stainless steel. This makes this research as an exploration of the potential of applying AISI 420 stainless steel welding wire for WAAM. In spite of the difference in the heat source some of the assumptions and results can be used as reference to guide this research.

2.1. Welding Parameters and Heat Treatment

2.1.1. Optimization of Welding Parameters

The parameters Current (A,amps), Voltage (V,volt), Wire Feed Rate (F, m/min), Welding Speed (S,m/min) and Stick - out (mm) are very crucial to obtain the desired weld bead geometry and properties for WAAM deposition. A properly calculated combination of the above parameters yields the best quality of the weld in terms of geometrical aspects such as Bead Width (W), Height (H) and Depth of Penetration (P) and metallurgical aspects such as defect free weld beads, less spatter and inclusions.

K.Y Benyounis et. al. [18] have compiled together the available statistical and numerical approaches to optimize welding parameters for various processes based on weld bead geometry and mechanical properties. The models that were studied are:

- Factorial Design
- Linear Regression
- Response Surface Methodology (RSM)
- Artificial Neural Networks (ANN)
- Taguchi Method

It was concluded that RSM model performed better than others in terms of computational time, optimization, accuracy level and application. In addition, a combination of two models such as ANN and Taguchi will provide great accuracy in predicting the resulting bead parameters.

Some other researchers that used statistical methods for prediction such as I.S. Kim et. al. [19] who performed experiments for predicting the bead height in robotic arc welding using neural networks. They developed an algorithm to establish relationship between the process parameters and dependent parameters. They used a series of multi - pass butt welds to verify the performance of the network. Their results showed accurate guarantee of prediction and also proved to be better than empirical models.

N. Murugan et. al. [20] researched on the effects of MIG process parameters on the geometry of bead in automatic surfacing of Stainless Steel. They developed a five - level factorial technique and developing models to predict weld geometry.

V. Gunaraj et. al. [21] employed the Response Surface Methodology (RSM) to predict weld quality in submerged arc welding of pipes. They developed a four - factor five - level central composite design matrix to achieve the desired weld qualities with the optimum combination of input parameters.

Apart from employing the above said mathematical and statistical models, another optimization procedure called the Paramteric Scanning was suggested by Ya [22]. This procedure has some advantages over the mathematical models in practice such as reduced number of test samples in a way that it is possible to output various input parameters' responses in one single weld bead. Visual inspection can then be made on the trials and narrow down to one desired weld condition. For example, along the length of the bead, the travel speed can be kept constant while the Current & Voltage is increased and decreased. This procedure is called the Energy Input ramping. And, the vice versa is called the Speed Ramping.

Selection of Shielding Gas

The shielding gas is very crucial during GMAW as it influences many factors such as surface appearance, weld geometry, corrosion resistance, metallurgy, mechanical properties and shielding efficiency [23]. It is recommended to use pure Argon or a mix of 98% Ar + 2% O_2 + He for a good quality weld due to it's good blend properties such as increased heat input and wettability [24]. The influence of shielding gas by it's mixture components is shown in *Figure 2.1*.

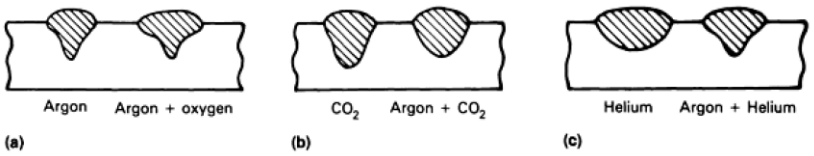

Figure 2.1: Effect of shielding gas on weld bead profile [24]

Phase Diagram [24]

Figure 2.2(a) below shows the binary Fe-Cr phase diagram. It indicates that alloys having (>12%) Cr, austenite will not form at any temperature. But, addition of C to Fe-Cr increases the range on which austenite can be formed at high temperatures *Figure 2.2(b)*. Other alloying elements such as Nitrogen, Copper, Nickel and possible Manganese can expand this range. A fully austenitic microstructure can be obtained with about 17% Cr and 0.4% C.

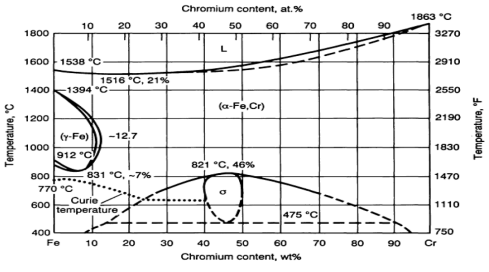

(a) Binary Iron Chromium Phase Diagram

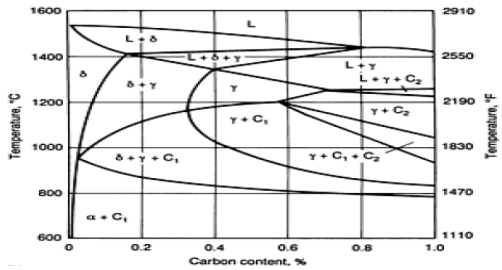

(b) Phase diagam isopleth of the Ternary Iron - Chromium - Carbon Diagram with 17% Cr

Figure 2.2: Phase Diagrams of Stainless Steel [24]

Figure 2.3 below shows the Isothermal Transformation Diagram for the 410 type stainless steel. It indicates that martensite begins to form (M_s) at 350°C and finishes when the cooling reaches 250°C. Alloying above 12% Cr delays the formation of ferrite and further reduces the martensite - start temperature. For 420 type stainless steel, the M_s is calculated from the *Equation 2.1.1* which is 98.6°C by substituting the chemical composition mentioned in *Table 1.1*.

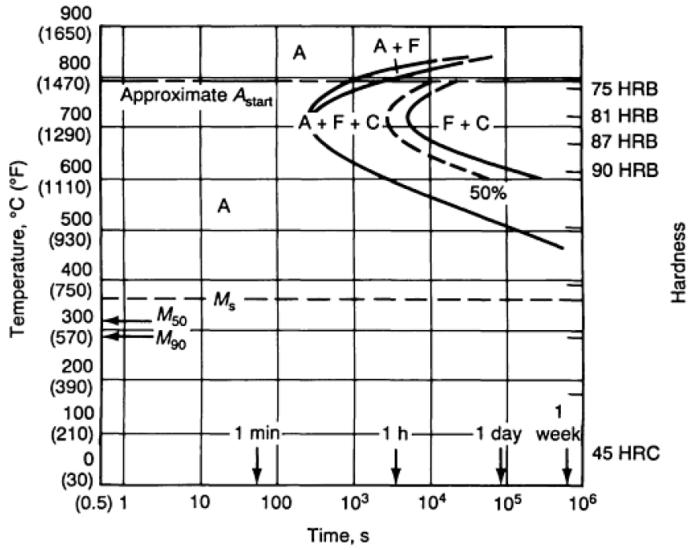

Figure 2.3: Isothermal Transformation Diagram of Type 410 Stainless Steel [24]

The ASM Handbook [24] also suggests that some austenite may exist indefinitely even at room temperatures and complex heat treatment procedures such as double tempering may be needed to induce complete martensite transformation in highly alloyed martensitic stainless steel.

Dr. G. Balachandran [25] also suggests that with 12% Cr and increasing C expands the austenite (γ) forming range. At 18% Cr, γ range decreases but addition of C, Mn, and Ni will widen the γ range. Finally at 17% Cr with low carbon forms ferrite.*Figure 2.6* shows the Fe - Cr phase diagram at 17% Cr and indicates that it is an austenite field with a possibility to form carbides.

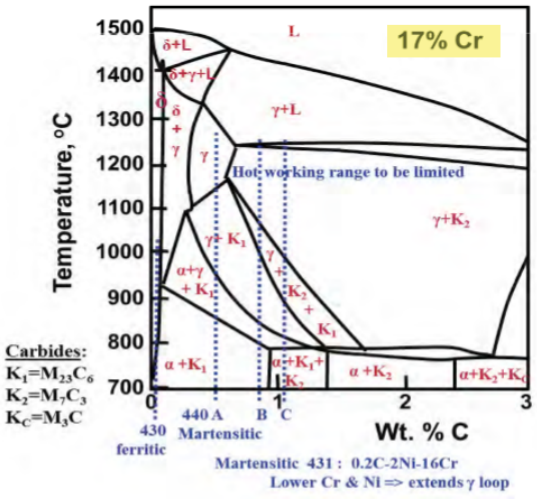

Figure 2.4: Fe - Cr Phase Diagram for 17% Cr [25]

The Martensite start temperature has been formulated by Beres et. al. [26] based on the concentration of

the various individual elements present in the MSS.

$$M_s = 540 - (497\text{x}\%C + 6.3\text{x}\%Mn + 36.3\text{x}\%Ni + 10.8\text{x}\%Cr + 46.6\text{x}\%Mo)°C \quad \text{(Eq. 2.1.1)}$$

Pre Weld Heat Treatment

Martensitic stainless steels are sensitive to cold cracking due to carbon and hydrogen concentration. Preheating is recommended to prevent cracking. It is advised to heat upto 400°C [23].

Hot cracking or solidification cracking [27] occurs in stainless steel due to eutectics containing impurities such as Sulphur, Phosphorous and alloy elements such as Ti and Nb. Nitrogen that is absorbed during welding enhances cracking and can be reduced by minimizing the ratio of Nb to that of C and N present.

Cracking susceptibility is determined by elemental segregation that occurs in the brittle temperature range (BTR). In simple terms, solidification cracking occurs when the strain on the weld pool is too high and the inability of the liquid metal to reach the regions between solidifying grains due to blockage or narrow channels [28].

They usually appear as large - weld metal cracks along the weld centreline. They also sometimes appear as microfissures in the weld metal or HAZ at the fusion line and perpendicular to it [24].

The Nickel Development Institute [29] also suggests to preheat at a range of 200 - 315°C. For this research, the preheat temperature was chosen as 200°C. As, there was almost no previous researches done on AISI 420 except for welding guides, that temperature was chosen as a start point.

Post Weld Heat Treatment

The post weld heat treatment is very much an integral step in the welding of MSS. It can be achieved through two methods [29]:

1. Anneal at 820°C followed by controlled cooling at 600°C at a rate of 10°per hour followed by air cooling.
2. Heat to 730 - 760°C with cooling as stated above.

Through this treatment, the weld is softened and toughened at the same time[30]. The hardness after PWHT as reported by Gooch et. al [31] was 400HV.

Effects of Pre and Post Weld Heat Treatment

Cehyun et. al. [32] investigated the effects of the heat treatment on martensitic stainless steels. They found that the post weld heat treatment causes martensite to be transformed into ferrite by tempering while forming carbides. The carbides are responsible for local softening in the weld metal and the HAZ after post weld heat treatment.

For a better quality of weld seam and a successful joint, the factors affecting the weld can be brought under control by the pre and post weld heat treatment. The interpass temperature must be maintained at 350°C for multi - pass welding or there is a risk of disrtortion in the soft zones of the weld as reported by the Welding guide by Mirrax and Assab [33].

2.2. Machinability

Wire Electrical Discharge Machining (WEDM) is usually preferred to machine martensitic steels [34] irrespective of the materials' microstructure, hardness, shape or toughness [35] WEDM produces better quality product as it eliminates the need for a preshaped electrode and the fact that it uses a microprocessor that always maintains a gap of 0.025 - 0.05 mm between the wire and the workpiece. This leads to parts that are machined with high level of accuracy.

Also Mirrax and Assab [33] suggests if EDM is performed in the hardened or tempered condition, the machined surface is to be covered with a re-solidified layer. It is also recommended to finish the EDM process with "fine-sparking" which is high frequency and low current. Then it should be polished or ground to remove the layer. The material then should be retempered at 25°C below the tempering temperature for optimal performance.

The EDM method has good outcome in terms of surface roughness, metal removal rate (MRR) and kerf [36].

With regards to conventional machining processes such as milling, the machining characteristics of martensitic stainless steels is influenced by the following variables:

1. Hardness Level: Higher hardness levels decreases the machinability of that particular alloy. Carpenter guide to machining [37] suggests that when the hardness is in the range of 248 - 302HB, it results in a good combination of tool life and machined surface finish.
2. Carbon Content: Increase in carbon content decreases the machinability due to the formation of abrasive chromium carbides [37].
3. Nickel Content: Increase in annealed hardness levels influences the machinability in alloys such as Type 414 and 431 due to higher Ni content than Type 410 in the annealed condition [37].

2.3. Microstructure

Ismail et. al [38] performed microstructural characterization on 431 type martensitic stainless steel using laser deposited coatings. They observed the following solidification structures (*Figure 2.5*). *Figure 2.5 (a)* shows the transversal cross - section where in planar growth at substrate - coating interface is observed and *Figure 2.5 (b)* shows cellular dendritic structure with columnar to equiaxed transition at the very top of the deposit.

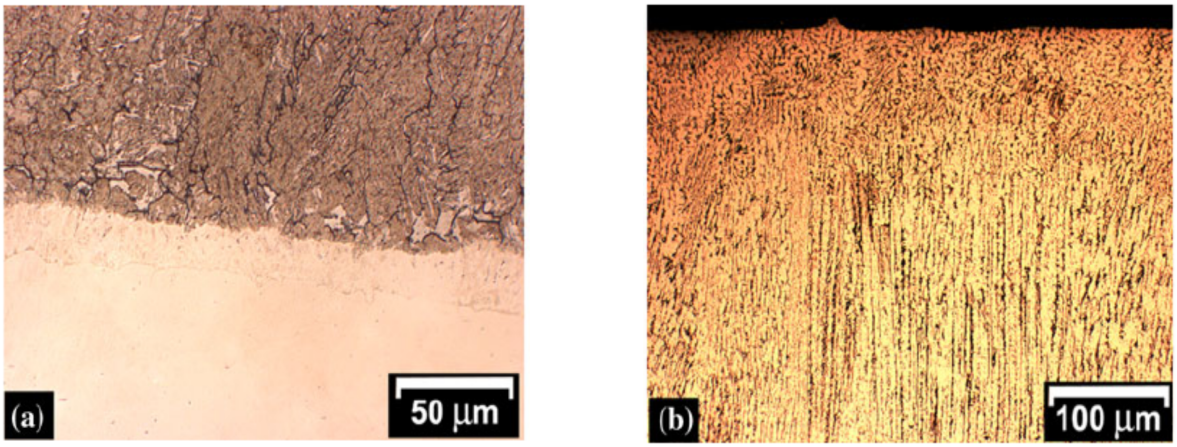

(a) Planar Growth at Substrate - Coating Interface

(b) Cellular Dendritic - Equiaxed Transition

Figure 2.5: Solidification Structures of 431 Martensitic Stainless Steel [38]

They further suggested that the formation of these solidification structures can be understood by the effect of solid - liquid interface growth rate R and temperature gradient in the melt (G). The G/R ratio determines the mode of solidification and the product (G.R) controls the scale of the structures as shown in *Figure 2.6.*

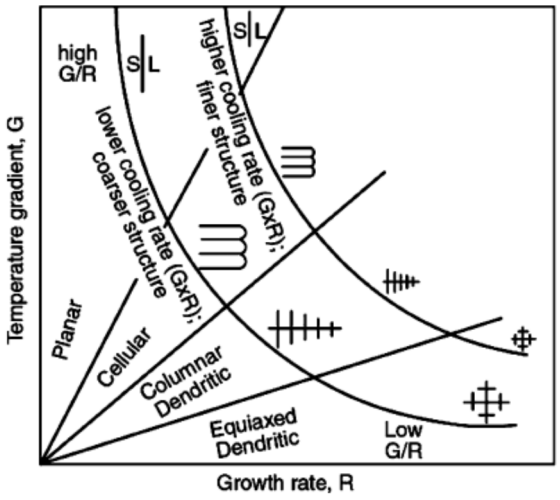

Figure 2.6: Effect of G and R on morphology and scale of solidification structures [38]

Barlow et. al [39] suggested that martensitic stainless steel is usually supplied in the fully annealed condition and that can be later heat treated by the user. Annealing is a process where the material is heated and held at a specific temperature and cooled down at a controlled rate to obtain specific microstructure, mechanical or physical properties, reduce hardness and improve machinability.

This produces fully ferritic matrix with carbon being precipitated as coarse, globular carbide particles in AISI 420. Randomly dispersed globular carbides ($M_{23}C_6$) in AISI 420 is shown in *Figure 2.7 (a)*. The SEM image of AISI 420 after annealing at 750°C for 2 hours consists of ($M_{23}C_6$) *Figure 2.7 (b)*.

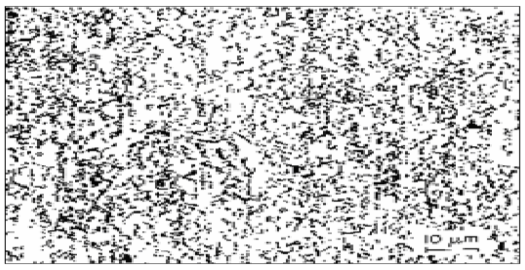

(a) Optical Micrograph of AISI 420 in Spheroidise Annealed Form

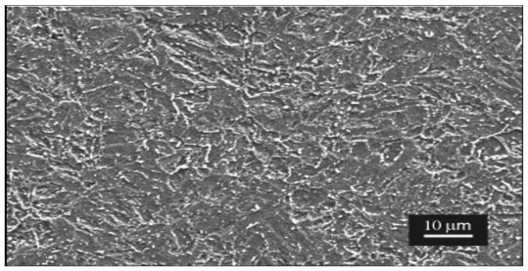

(b) SEM Micrograph of Annealed AISI 420 at 750°C for 2 hours

Figure 2.7: Optical and SEM Micrograph of AISI 420 Stainless Steel [39]

The samples were etched using the Vilella's reagent that consists of 1 gram of Picric Acid, 5 ml HCl and 100 ml Ethanol. This is specifically used for ferrite - carbide structures in iron and steel. Another etchant that is recommended for duplex and 400 series stainless steel is the Kalling's No. 2. This etchant will darken martensite, attacks ferrite quickly and slightly etch austenite as suggested by the ES Laboratory, an etchant manufacturer [40] and by the article on Guide to Etching Speciality Alloys [41].

2.4. Microhardness

As far as martensite is concerned, the hardness is determined by the carbon content in the alloy. *Figure 2.8* below shows the influence of carbon and hardness levels determined experimentally [24]. It shows that at a minimum of 0.1%C, the hardness value is approximately 35HRC (~ 332HV) and reaches a maximum of

60HRC (>746HV) at 0.5%C if 100% martensite is achieved in the steel. The AISI 420 used in this research has a carbon content of 0.38%. From the figure, the weld metal is expected to have a hardness of approximately 50HRC (~ 505HV). This is also the maximum requirement of hardness level for moulds made with AISI 420 as mentioned earlier in *Section 1.3*.

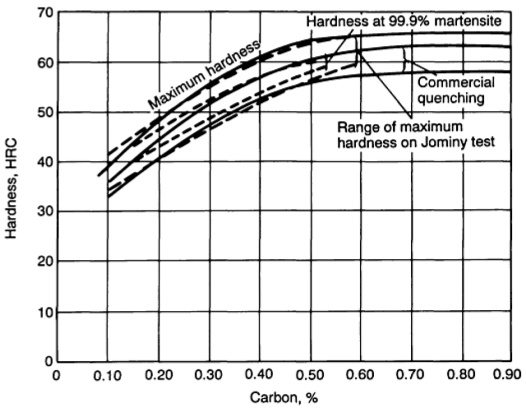

Figure 2.8: Hardness of martensite Vs %C [24]

2.5. Summary

Based on the literature study, Response Surface Methodology (RSM) is considered to be used for process optimization. By studying the parametrical effects of the weld geometrical characterizations, proper process conditions can be selected for studying the potential of applying WAAM on AISI 420 stainless steel. Through statistical analyses the processing conditions and the weld geometrical characterizations, the correlations between processing parameters and the responses are expected to be found. Eventually, further correlations between the process conditions and resulting microstructure can be investigated. Research carried out in this work are detailed in following chapters.

3

Experimental Setup, Material Used and Design of Experiments

The aim of this experiment is to obtain optimal process conditions for the WAAM deposition of AISI 420 stainless steel. In this chapter the experimental setup used for the deposition is briefly introduced. The focused deposition material is AISI 420 stainless steel as its various applications to be explored with WAAM process, and there are industrial interests mentioned in *Chapter 1, Section 1.3.* Although welding of AISI 420 with traditional Gas Metal Arc Welding (GMAW) process has been investigated [23, 42, 43], using AISI 420 stainless steel welding wire for additive manufacturing 3D components is yet to be explored. As proposed by many other researchers [44–48], to avoid trials and errors method, the cost effective and reliable method to obtain optimal processing conditions is through Design of Experiment (DoE) with adequate statistical analysis. It is also commonly known as Response Surface Methodology (RSM), which is a topic that covers broad range of DoE methods and statistical approaches. The methods used in this study are detailed in the following sections.

3.1. Experimental Setup

A Panasonic TM1400 MIG Welding robotic system from Valk Welding was used to perform experiments (*Figure 3.1 (a)*). ARCAL - 121 shielding gas was used which is a mixture of 80% Argon, 18% He and 2% CO_2. Helium and CO_2 is mixed with Ar to improve the heat input delivery which increases the wetting, weld bead profile and puddle fluidity. Since CO_2 is relatively low (<5%), the stainless steel is welded without any loss in corrosion resistance as reported in *Section 2.1.1* [23] [24]. Preheating is performed during welding experiments with a cooking hot plate and temperature was monitored (*Figure 3.2 (b)*) with a k-type thermocouple which bonded on the substrate plate with a thermal paste (Thermofix 1000°C). The weld bead was deposited on the substrate with a length of 155 mm to obtain steady state of welding conditions, while substrate was clamped. Subsequently, cross sections at the centre of the welds were prepared through standard metallographic procedures.

(a) Panasonic TM1400

(b) Weld Setup

Figure 3.1: Welding Robot and Preheat Setup

3.2. Material Used

The AISI 420 martensitic stainless steel welding wire with a diameter of 0.9mm was produced by Weld Mold Co. (USA) moulding company as shown in *Figure 3.2*. The AISI 420 stainless steel is deposited on substrate through active wire production method [49, 50]. The chemical compositions of the welding wire and substrate (in wt.%) are shown in *Table 3.1*. The dimension of the substrate was 250 x 60 x 10 mm.

Figure 3.2: 0.9mm ϕ Stainless Steel 420 Spool

Table 3.1: Chemical Composition of wire used wt.%

Material	C	Cr	Fe	Mn	Mo	Ni	Si
AISI 420	0.38	16	80.77	0.65	1.0	0.8	0.4
S355J2	0.22	-	96.55	1.6	-	-	0.55

3.3. Process Optimization

Considering that limited researches were previously reported on WAAM process using AISI 420 stainless steel, there is a need to find a suitable methodology for process optimization during WAAM deposition of the AISI 420 stainless steel. In principal, this approach can also be applied for other materials. The Response Surface Methodology (RSM), based on its advantages compared to other methodologies mentioned in *Section 2.1.1*, explores the relationships between several "explanatory variables" and one or more "response variables" [21]. The RSM can be used as a predictive technique that is able to determine and represent the relationships between the input (Current, Voltage and Travel Speed) and the variables (Width, Height and Depth of Penetration).

To achieve the desired aim, the present study has been made in the following steps:

1. Determine the main processing parameters
2. To find out the upper and lower limits of the considered parameters
3. Developing an experimental design matrix
4. Conducting the experiments based on the design matrix
5. Recording and analysing the responses
6. Developing the statistical model
7. Checking the adequacy of the developed statistical model
8. Experimental validations

3.3.1. Main Process Parameters and Responses

According to the literature [44–48], the main processing parameters affecting the weld bead shape and penetration of the weld are welding Current (A), Voltage (V), Travel Speed (S), shielding gas flow rate, and inclination of the welding torch. In this study, the shielding gas flow rate is fixed at 18 l/min as it gives the most stable arc and the least spatter according to our preliminary experimental observations. A deposition strategy limitation, required in additive manufacturing, is that the processing tool should be always normal to the working plane; thus the inclination is chosen to be constant at 90 degrees. Therefore, welding Current (A), Voltage (V) and Travel Speed (S) are considered as the main processing parameter variables in this study and welding geometrical characteristics are considered as the responses including weld Width (W), Height (H) and Depth of Penetration (DoP). *Figure 3.3* shows a schematic cross section of a weld including the responses mentioned.

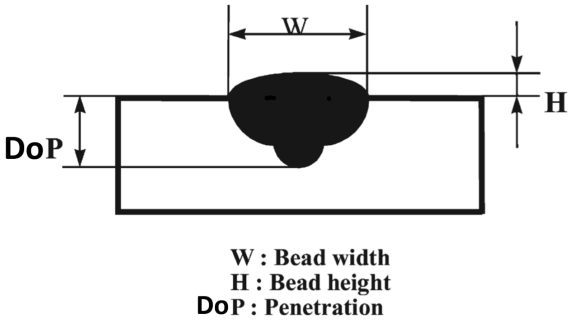

Figure 3.3: Weld Bead Parameters [51]

3.3.2. Limits of the Main Processing Parameters

Considering the limitations of the robot system and the welding parameters recommendation (180 - 320 A of current and 23 - 29 V of voltage) from the stainless steel manufacturers catalogue [52], the boundaries of the processing conditions were initially selected. The upper limit was coded as +2 and the lower limit as -2. The other coded values in between are calculated from the following equation [21] as follows:

$$X_i = \frac{2[2X - (X_{max} + X_{min})]}{(X_{max} - X_{min})} \quad \text{(Eq. 3.3.1)}$$

where,

X_i is the required coded value of variable X;

X is any value of the variable from X_{min} to X_{max}

The calculated coded limits of the parameters are given in Table 3.2.

Table 3.2: Input parameters and their limits

Parameters	Units	Notation	Limits				
			-2	-1	0	+1	+2
Current	Ampere	A	180	215	250	285	320
Voltage	Volts	V	23.0	24.5	26.0	27.5	29.0
Travel Speed	m/min	S	0.30	0.45	0.60	0.75	0.90

3.3.3. Design of Experiments (DoE) - Design Matrix

In most RSM problems, the true response function $f(x_1, x_2, \epsilon)$ is unknown. In order to develop a proper approximation for $f(x_1, x_2, \epsilon)$, the experimenter usually starts with a low-order polynomial in some small region. If the response can be defined by a linear function of independent variables, then the approximating function is a first-order model. A first-order model with 2 independent variables can be expressed as Eq.3.3.2.

If there is a curvature in the response surface, then a higher degree polynomial shall be used. The approximating function with 2 variables is called a second-order model Eq.3.3.3 [47].

$$f(x_1, x_2, \epsilon) = b_0 + b_1 x_1 + b_2 x_2 + \epsilon \quad \text{(Eq. 3.3.2)}$$

$$f(x_1, x_2, \epsilon) = b_0 + b_1 x_1 + b_2 x_2 + b_{12} x_1 x_2 + b_{11} x_1^2 + b_{22} x_2^2 + \epsilon \quad \text{(Eq. 3.3.3)}$$

where x_1, x_2 are the variable, b_i and b_{ij} (i,j=1,2,...) are fitting coefficients, and ϵ is the error.

In general, all RSM problems use either one or the mixture of the both models. In each model, the levels of each factor are independent of the levels of other factors. To get the most efficient result in the approximation of polynomials, the proper experimental design must be used to collect data. Once the data are collected, the method of least square is used to estimate the parameters in the polynomials. The response surface analysis is performed by using the fitted surface [47].

The design matrix shown in *Table 3.3* is a central composite rotatable factorial design consisting of 17 coded conditions. This design gives the freedom to have samples in the entire range of the limited input parameters. A full replication of 2^3 (=8) factorial design plus 3 centre points with variables at their intermediate level (0) plus 6 star points with combinations of variables at either their lowest (-2) or highest (+2) levels. Thus 17 experimental runs are carried out to estimate the relation between the input and the response variables.

Table 3.3: Design Matrix

Sample No.	Design Matrix			Code Conversion		
	Current	Voltage	Weld Speed	Current	Voltage	Weld Speed
1	-1	-1	-1	215	24.5	0.45
2	+1	-1	-1	285	24.5	0.45
3	-1	+1	-1	215	27.5	0.45
4	+1	+1	-1	285	27.5	0.45
5	-1	-1	+1	215	24.5	0.75
6	+1	-1	+1	285	24.5	0.75
7	-1	+1	+1	215	27.5	0.75
8	+1	+1	+1	285	27.5	0.75
9	-2	0	0	180	26	0.6
10	+2	0	0	320	26	0.6
11	0	-2	0	250	23	0.6
12	0	+2	0	250	29	0.6
13	0	0	-2	250	26	0.3
14	0	0	+2	250	26	0.9
15	0	0	0	250	26	0.6
16	0	0	0	250	26	0.6
17	0	0	0	250	26	0.6

3.3.4. Performing Welding Experiments According to the Design Matrix

The experiments were conducted as per the design matrix with two weld beads in one substrate. Temperature of the substrate was monitored with thermocouple to ensure that each experiment was performed when the substrate plate was heated up to 200°C. The performed experiments are shown in *Figure 3.4*.

3.3.5. Recording and Analysing the Responses

The welds shown in *Figure 3.4* were cut exactly half their length (75 mm, transverse direction). The cut samples were cold mounted and ground sequentially from 180, 320, 500 and 1000 grit sand papers in Tegramin - 30 grinding and polishing machine by Struers. Polishing was done from 9μ, 3μ to 1μ. They were subsequently etched using the etchant Kalling II which is a mixture of 100ml HCL, 100ml Ethanol and 5g $CuCl_2$.

Figure 3.4: Welded Test Samples

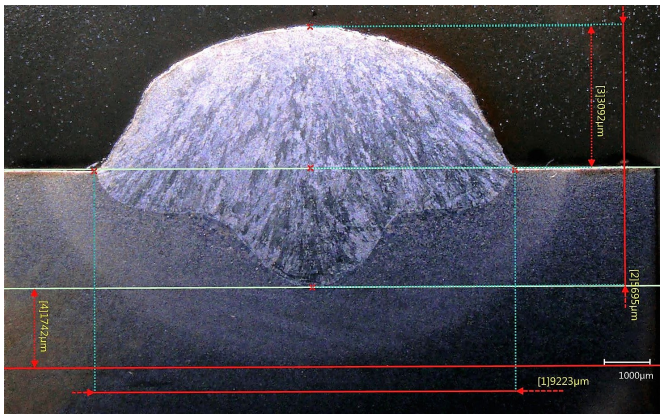

Figure 3.5: Measurement of bead parameters

The weld bead profile was traced using PlotDigitizer Software along with the measurement of weld bead parameters - Width, Height and Depth of Penetration as shown in *Figure 3.5* using VHX Keyence optical microscope. In *Figure 3.4*, it is shown that some weld beads are non uniform, meaning that they have varying bead widths along the length of the weld due to unsuitable welding parameter combinations in the design matrix. Only those weld beads that are uniform (1, 2, 3, 4, 7, 12, 13, 15 & 16) are considered for calculating the next steps. The recorded bead parameters are tabulated in Table 3.4.

Table 3.4: Input parameters and their bead parameters

S. No.	Sample No.	Current	Voltage	Speed	Width	Height	DoP
		A	V	m/min	mm	mm	mm
1	1	215	24.5	0.45	9.22	3.11	5.70
2	2	285	24.5	0.45	8.28	3.13	2.44
3	3	215	27.5	0.45	9.39	3.44	2.56
4	4	285	27.5	0.45	9.63	3.63	3.35
5	7	215	27.5	0.75	7.80	2.87	2.14
6	12	250	29.0	0.60	9.51	3.09	3.12
7	13	250	26.0	0.30	9.51	4.24	3.01
8	15	250	26.0	0.60	8.66	3.30	2.55
9	16	250	26.0	0.60	7.93	3.27	2.37

3.3.6. Mathematical Models: Regression Analysis

The relation representing any of the weld parameters can be expressed as $Y = f(A, V, S)$. The relationship being a regression function is given by:

$$Width = b0 + b1(A) + b2(V) + b3(S) \quad \text{(Eq. 3.3.4)}$$

$$Height = b0 + b1(A) + b2(V) + b3(S) \quad \text{(Eq. 3.3.5)}$$

$$DoP = b0 + b1(A) + b2(V) + b3(S) \quad \text{(Eq. 3.3.6)}$$

The coefficients b0, b1, b2 and b3 are estimated using the statistical Analysis Software - SAS [19]. The values of the corresponding coefficients are given in Table 3.4. The final mathematical model with the coefficients is given by:

$$Width = 4.1405–0.0029(A) + 0.3039(V)–5.0426(S) \quad \text{(Eq. 3.3.7)}$$

$$Height = 2.4481 + 0.0008(A) + 0.0778(V) - 2.6519(S) \quad \text{(Eq. 3.3.8)}$$

$$DoP = 12.666–0.0145(A)–0.1683(V)–3.1204(S) \quad \text{(Eq. 3.3.9)}$$

Table 3.5: Estimated coefficients

S. No.	Coefficient	Width (W)	Height (H)	Depth of Penetration (DoP)
1	b0	4.1405	2.4481	12.666
2	b1	-0.0029	0.0008	-0.0145
3	b2	0.3039	0.0778	-0.1683
4	b3	-5.0426	-2.6519	-3.1204

3.3.7. Optimal Welding Condition

Since, this research is aimed towards producing or repairing defective moulds for ceramic bath tubs, the material deposited is not more than two layers. This is known as Cladding or Surface Coating. In order to achieve faster deposition rates, the response parameters are optimised for maximum width, minimum height and minimum DoP. Maximum width helps to quickly coat the surface, minimum height specifies the thickness of the deposition.

Data from the *Table 3.4* and *Equations 3.3.7 - 3.3.9* were specified as input to the statistical software Minitab. The combination of required response parameters were specified and Minitab performs a fit through regression analysis and outputs the optimal condition which is shown in *Table 3.6*.

Table 3.6: Optimal Condition (OC)

Current A	Voltage V	Travel Speed m/min
261	29	0.59

3.4. Single Weld and Overlapped Weld

With the obtained OC, a single bead on plate test as shown in *Figure 3.6* was performed. It was then cross sectioned in half in the transverse direction, ground, polished, etched and observed under an optical microscope *Figure 3.7*. The predicted and measured bead parameters are given in *Table 3.7*.

Figure 3.6: Optimal Condition's Weld Bead

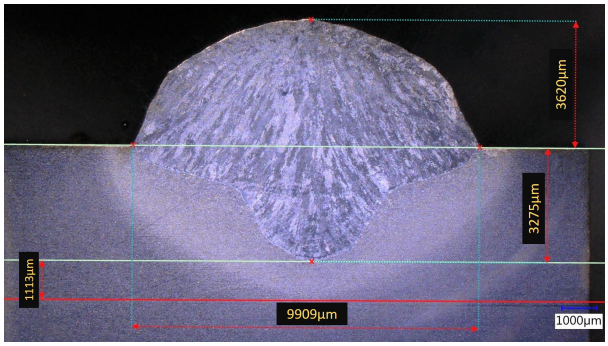

Figure 3.7: OC Weld Bead and it's Response (Width, Height and DoP) Parameters

Table 3.7: Predicted Vs Measured Bead Parameters

Optimal Condition (OC)			Predicted			Measured		
Current	Voltage	Travel Speed	Width	Height	DoP	Width	Height	DoP
A	V	m/min	mm	mm	mm	mm	mm	mm
261	29	0.59	9.18	3.33	2.13	9.9	3.6	3.2

Subsequently, the experiments of the overlapped weld were performed with obtained welding conditions. Experiments were performed at different overlap ratio (33%, 50% and 60%). The overlap ratio is defined as OR=(Weld width - lateral displacement)*100% / weld width). The cross sections of the overlapped welds were prepared as shown in *Figure 3.8*. As large porosities and non uniform surface were found in the overlapped weld, it was concluded that obtained optimal condition (OC) may be suitable for single weld but not applicable overlapped welding where the additive manufacturing is required. Further process optimization is required.

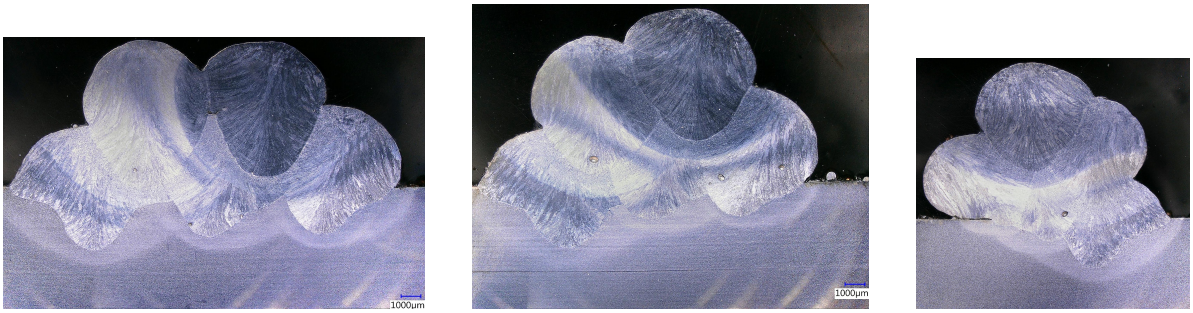

(a) 33% Over Lap (b) 50% Over Lap (c) 60% Over Lap

Figure 3.8: Tested Over Lap Ratios

3.5. Parametric Scanning and RSM

The combination of parametric and RSM has been applied to obtain optimal conditions for laser cladding by Ya [22]. The advantage of this method are 1. Minimizing the experiments by parametric scanning (ramping the input parameters during process); 2. Understanding the relationship between input parameters and responses; 3. Find the optimal process condition rapidly and efficiently with RSM. The following sections details the application of this method.

3.5.1. Parametric Scanning - The Input Parameter Ramping

The term *Ramping* is defined as a procedure when either one of the input parameters is dynamically changed (increased or decreased) during welding. This provides multiple bead morphologies in one single weld bead.

(a) Speed Ramping

(b) Energy Input Ramping

Figure 3.9: Ramping Procedures

3.5.2. Limits of Input Parameters

As the limits defined based on the welding parameters recommendation from the stainless steel manufacturers catalogue [52] are not suitable for obtained the optimal process conditions for additive manufacturing, the testing limits are expanded starting with 120 A, 16.4 V and 0.2 m/min as the lowest limit to 280 A, 19.6 V and 1.0 m/min as the upper limit.

3.5.3. Ramping Experiments

Two sets of ramping procedures were performed and each containing five different parameter sets:

1. Constant Current and Voltage with Ramping up the Travel Speed and,

2. Ramping up and down the Current and Voltage with constant Travel Speed.

Tables 3.8 and 3.9 below show the setup for each of the two procedures above.

Table 3.8: Constant A & V with ramped up S

Current A	Voltage V	Travel Speed m/min
120	16.4	0.20
120	16.4	0.24
120	16.4	0.28
120	16.4	0.32
120	16.4	0.36
120	16.4	0.40
120	16.4	0.44
120	16.4	0.48
120	16.4	0.52

Table 3.9: Constant S with ramped up & down A,V

Current A	Voltage V	Travel Speed m/min
140	16.7	0.2
180	18.0	0.2
220	19.3	0.2
240	20.8	0.2
280	24.4	0.2
240	20.8	0.2
220	19.3	0.2
180	18.0	0.2
140	16.0	0.2

3.5.4. Performing the Experiment

Single bead on plate welding with parameter ramping was performed with a length of 160 mm. The weld contained 10 points separated by a distance of 20 mm from start to end. The input parameters were changed between those points so that each input condition's resulting weld bead morphology can be visualized. Examples are shown in *Figure 3.10*.

The start of the weld is on the right. The variation in the bead's width can be seen in the bottom bead of the figure.

Figure 3.10: Resulting Weld Bead of constant S with ramped up & down A & V

3.5.5. Recording Responses

Height (H) and Width (W) of all the beads in those 10 sets were measured and tabulated in *Table 3.10*.

Table 3.10: Measured Bead Parameters

Current A	Voltage V	Travel Speed m/min	Width W	Height H
120	16.4	0.20	7.9	4.5
120	16.4	0.24	4.6	3.6
120	16.4	0.28	4.3	3.6
120	16.4	0.32	4.2	3.6
120	16.4	0.36	3.5	3.1
120	16.4	0.40	3.6	3.9
120	16.4	0.44	3.3	3.9
120	16.4	0.48	4.1	2.6
120	16.4	0.52	4.4	2.4

3.5.6. Mathematical Modelling

As all the observed samples show no detachment and relatively smooth surface, all welding conditions used can assure the minimum bonding. The model development focuses on the weld width and height. The third order polynomial (regression) equation [22] used to represent the response surface of weld width and height is given by:

$$y_i = \beta_0 + \sum_{j=1}^{k} \beta_j x_j + \sum_{j}^{k} \beta_{jj} x_{jj}^2 + \sum_{i}^{i<j} \sum_{j=2}^{k} \beta_{ij} x^i x^j + \epsilon \qquad \text{(Eq. 3.5.1)}$$

where β_0 is a constant, β_j is the j^{th} linear coefficient, β_{jj} is the j^{th} quadratic coefficient, β_{ij} is the i^{th} interaction coefficient, x_j is the independent variable (P_v, v_c and $\dot{m}$), k is the number of factors and ϵ is the associated error.

$$\begin{aligned} Width = & -5.504 + 0.078 * C + 0.2 * V + 7.431 * S \\ & - 0.131 * C * S - 1.044e - 004 * C^2 \\ & + 3.414 * S^2 + 0.105 * C * S^2 \\ & - 11.323 * S^3 \end{aligned} \quad \text{(Eq. 3.5.2)}$$

$$\begin{aligned} Height = & 5.554 + 7.858e - 003 * C - 15.303 * S + 4.035e - 003 \\ & * C * S + 18.458 * S^2 - 8.669 * S^3 \end{aligned} \quad \text{(Eq. 3.5.3)}$$

where 'C' is the welding current, 'V' is the welding voltage and 'S' is the welding / travel speed.

Through Analysis of variance (ANOVA) of the recorded weld width and height, the model statistics are summarized in *Tables 3.11 and 3.12*. The detailed ANOVA are described in literatures [53, 54]. The obtained mathematical expression of weld width and height are expressed as following.

Table 3.11: Model statistics summary of weld width

Std. Dev	0.28	R-Squared	0.9577
Mean	5.22	Adj R-Squared	0.9442
CV%	5.32	Pre R-Squared	0.8936
PRESS	8.10	Adeq Precision	36.764

Table 3.12: Model statistics summary of weld height

Std. Dev	0.23	R-Squared	0.9508
Mean	3.66	Adj R-Squared	0.9420
CV%	6.16	Pre R-Squared	0.9321
PRESS	1.97	Adeq Precision	35.93

From *Tables 3.11 and 3.12*, the "Pred. R-squared" of 0.8936 for weld width and 0.9321 for weld height are in agreement with the "Adj. R-squared" of 0.9442 for weld width and 0.9420 for weld height. "Adeq precision" quantifies the signal to noise ratio. A ratio greater than 4 is desirable, the value of "Adeq precision" is 40.15 that indicates an adequate signal. Therefore, this model can be used to navigate the design space. The graph of predicted bead height and actual bead height is shown in *Figure 3.11*.

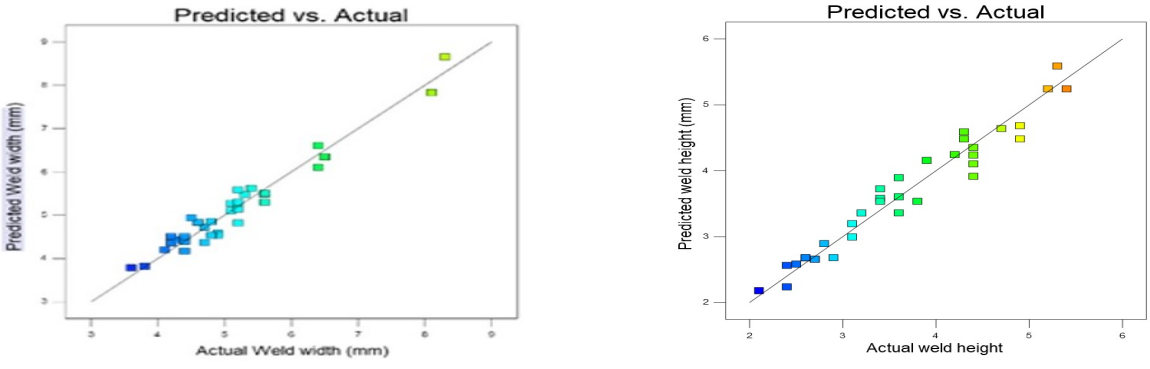

(a) Weld Width (b) Weld Height

Figure 3.11: Predicted Vs Actual values

Table 3.13: Set up at which weld bead satisfies the conditions

Sample No.	Current A	Voltage V	Travel Speed m/min	Width W,mm	Height H,mm
1	140	16.7	1.0	5.1	2.8
2	180	18.0	1.0	3.8	2.1
3	220	19.3	1.0	4.9	2.7
4	240	20.8	1.0	4.5	2.8
5	280	24.4	1.0	5.6	2.6
6	240	20.8	1.0	5.2	2.4
7	220	19.3	1.0	4.8	2.7
8	180	18.0	1.0	4.5	2.4
9	140	16.0	1.0	3.7	2.2

Figure 3.12: The resulting weld bead from Table 3.13

The data shown in *Table 3.13* was at which the appropriate welding conditions were seen with less spatter and faster deposition. The (OC - R) condition was chosen to be 200V, 18.5A and 1.00m/min in reference to the statistical analysis performed. The corresponding weld bead from *Table 3.13* is shown in *Figure 3.12* and the single bead OC - R condition's weld bead is shown in *Figure 3.13*. The 5 samples (2 - 5) including the optimal condition (OC - R) were ground, polished and etched to record it's parameters under an optical microscope shown in the results chapter.

Figure 3.13: The OC - R condition

Hardness Measurement:

The samples were measured for their hardness levels using a Vickers hardness testing machine with 1kgf load and 40X objective lens. Their results are shown in *Chapter 4*.

SEM Analysis:

The samples were observed under a Scanning Electron Microscope to study it's microstructural characteristics shown in *Chapter 4*.

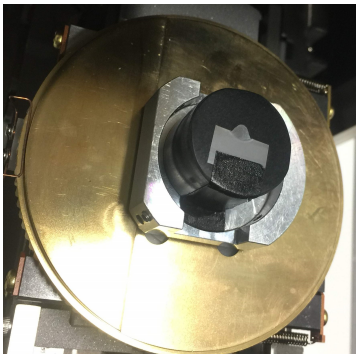

Figure 3.14: SEM Setup

3.6. Additive Manufacturing with OC - R

3.6.1. Coating (or) Surface Cladding

As the request from the industrial partner, *Figure 3.15* shows that the substrate is deposited with 2 layers of the AISI 420 stainless steel on the surface of S355J2. The obtained optimal conditions (OC - R condition) were used during the deposition. This is typical for repairing a defected mould by surface coating. The step over and step up were 2.5 and 2 mm respectively. This method complies with the requirements of Villeroy & Boch to produce or restore defective moulds for their end products. This procedure requires less time than to make an entirely new mould. The restored mould can then be machined and re - polished for a reuse.

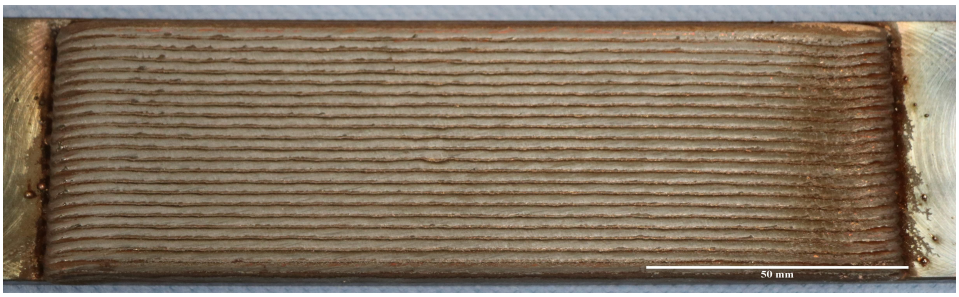

Figure 3.15: Cladding of AISI 420

3.6.2. Building Walls

The OC - R condition was further tested by building multi - layered components. At first a rectangular block with the dimensions 150 X 50 X 20 mm was modelled in CAD and then built using the Powermill software. Two blocks were deposited with different weld tool paths for comparison. The difference of the weld path is explained in the following paragraph.

1. Oscillation Strategy:

   In this strategy, the weld path follows as shown in *Figure 3.16*. The direction of the weld path is reversed for every alternate layer. This is to build up constant height otherwise the height on one side will be higher than the other. For the oscillated weld path, the program consisted of 25 layers and took approximately 45 minutes to build the near - net shape as the model. The build was then cut in transverse and longitudinal directions to observe its build quality. The produced sample is shown in *Figure 3.17*.

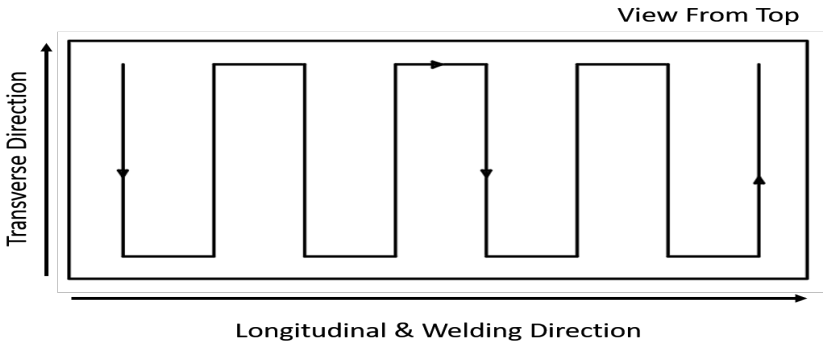

Figure 3.16: Oscillation Strategy

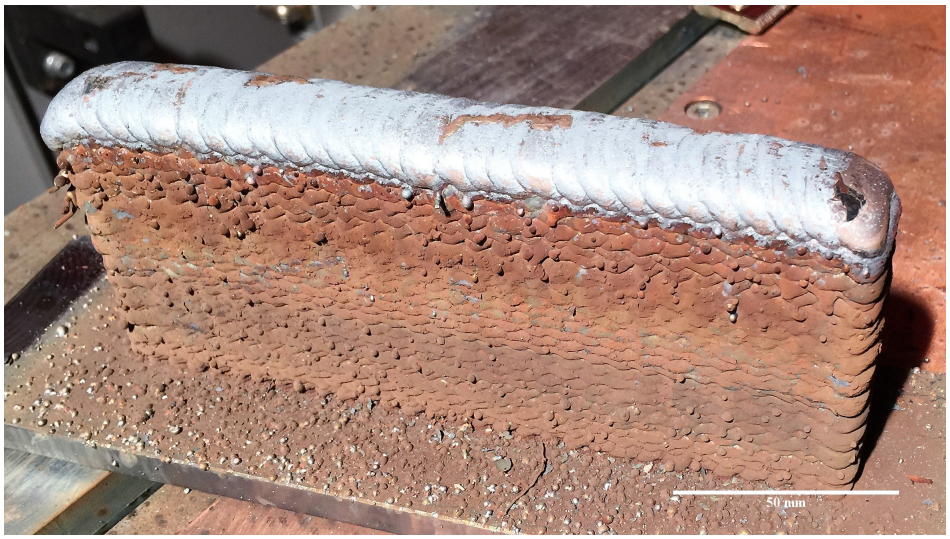

Figure 3.17: Oscillation Strategy - Build

2. Straight line with alternative welding directions:

For the straight line strategy, the start and stop points are reversed for every adjacent weld bead as shown in *Figure 3.18*. The weld path follows a straight line that is within the boundaries of the model. As the oscillation strategy, this contains 25 layers as well and the time to build this part took approximately 1.5 hours. The build was then cut in the transverse direction to identify any presence of weld defects and build quality. The deposited sample is shown in *Figure 3.19*.

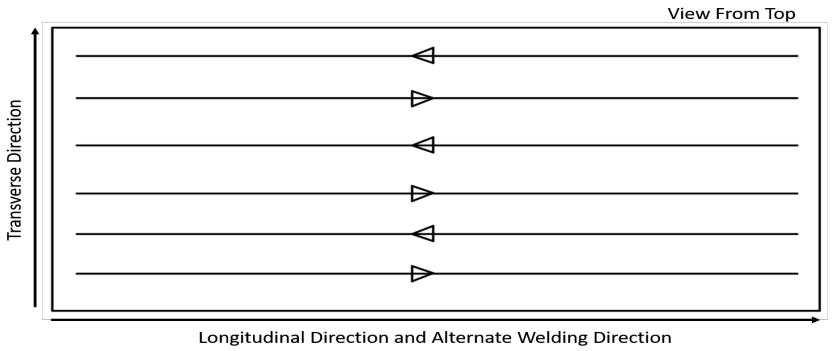

Figure 3.18: Straight line with alternative welding directions

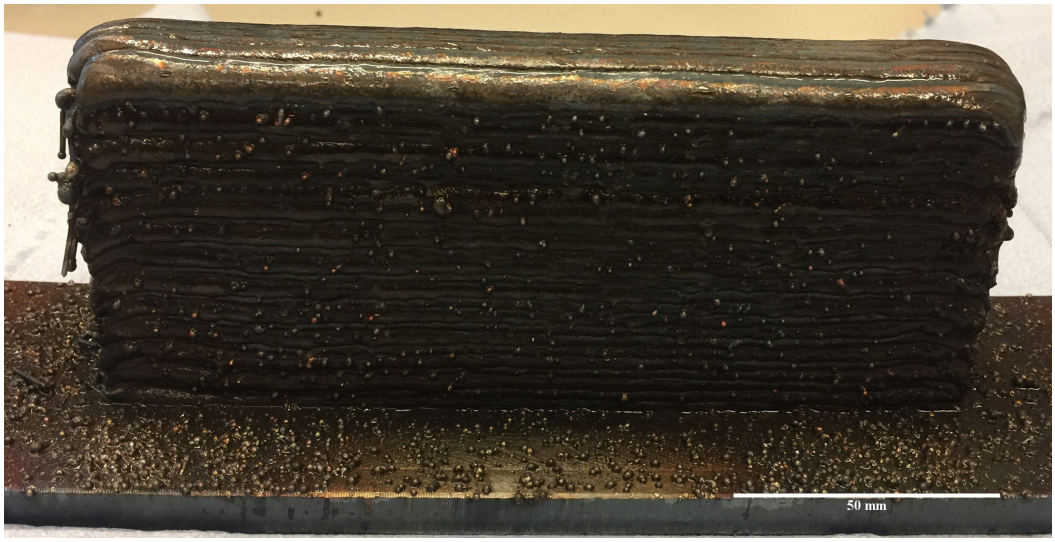

Figure 3.19: Straight line with alternative welding directions

3.7. Summary

Experimental procedures were carried out to achieve the aims of this research mentioned in *Section 1.3*.

Response surface methodology (RSM) was applied to obtain the optimal condition of the input parameters which was found to be 261A, 29V and 0.59m/min (OC). Preheating was done at 200°C and although post weld heat treatment was suggested in *Chapter 2*, it was not carried out as the resulting hardness has been met with the machinability requirements (as mentioned earlier in *Chapter 1, Section 1.3*) for the mould which will be discussed in *Chapter 4 and 5*. This weld condition however was found suitable only for single weld applications and not for additive manufacturing. This is due to the presence of large amount of spatters produced during welding, huge pores and non uniform surface characteristics.

Investigation was carried on further using the parametric scanning methodology. It had advantages over RSM such as less number of experiments due to the ramping procedure and finding the optimal condition rapidly and efficiently. The optimal condition found with this method was 200A, 18.5V and 1.00m/min (OC - R). This condition's weld bead had smooth surface quality, less spatter produced and has a faster deposition rate. One of the more interesting fact is that this condition did not require preheating.

The OC - R condition was then employed in cladding which is a build containing 2 layers of the material deposited on the substrate. The resulting build was flat on the surface and did not produce any spatters as expected. Multi - layered block or walls were also built using two path strategies - Oscillation and straight line with alternate welding directions. The oscillation strategy took 45 minutes to complete and was faster than the other strategy which took nearly 1.5 hours to complete.

4

Results

This chapter consists only the results and observations made during the experimental procedures. Discussion on these results is presented in *Chapter 5*.

4.1. Optimal Condition (OC)

This section contains the results and other findings or observations based on RSM.

4.1.1. Input Parameters

From the systematic and mathematical approach of Response Surface Methodology (RSM), the optimized input parameters or the proper combination of Current, Voltage and Travel Speed according to *Equation 3.3.7 - 3.3.9* is

Table 4.1: Optimal Condition (OC)

Current A	Voltage V	Travel Speed m/min
261	29	0.59

4.1.2. Bead Parameters

Figure 4.1 shows the cross section of the weld deposited at the OC condition. The height, width and depth of penetration were measured and compared to its predicted parameters in the RSM. The compared results are listed in *Table 4.2*. The height and width agree well with the prediction. However, the depth of penetration is not accurate.

Table 4.2: Predicted and Measured Values of Bead Parameters

Optimal Condition (OC)			Predicted			Measured		
Current A	Voltage V	Travel Speed m/min	Width mm	Height mm	DoP mm	Width mm	Height mm	DoP mm
261	29	0.59	9.18	3.33	2.13	9.9	3.6	3.2

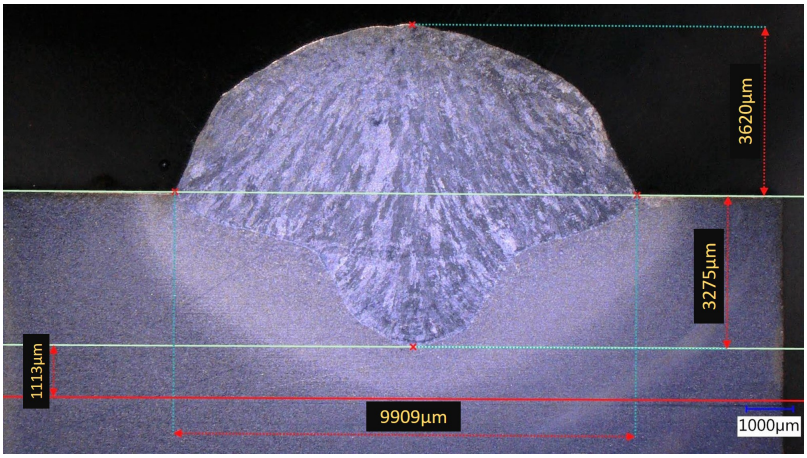

Figure 4.1: OC Weld Bead and it's Dependent Parameters

4.1.3. Hardness

The Vickers hardness test with 1kgf, 40x objective and 20 points of measurement across the weld bead resulted in a hardness value of 514 HV for the weld metal, 263 HV for the Heat Affected Zone (HAZ) and 183 HV for the substrate. The hardness profile is shown in *Figure 4.2*.

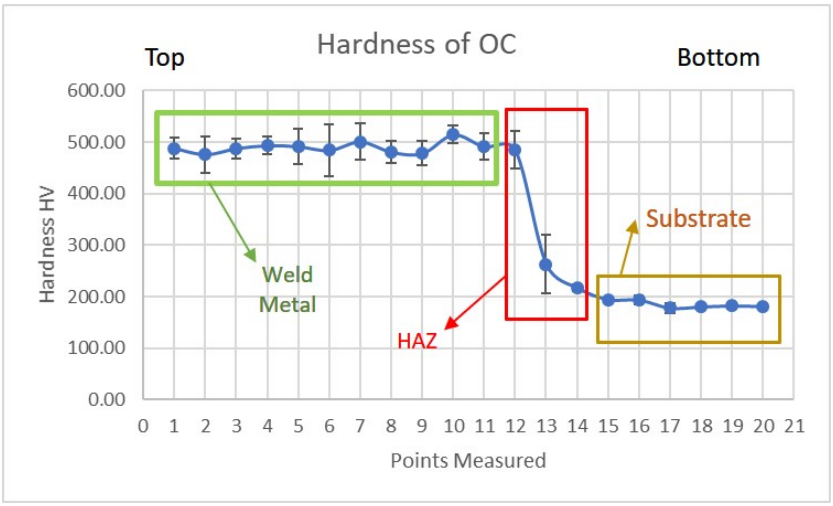

Figure 4.2: Hardness profile of OC single bead weld

4.1.4. Microstructure

The microstructure of the OC weld bead consisted traces of δferrite in a martensite matrix. See *Chapter 5* for the microstructural characterization.

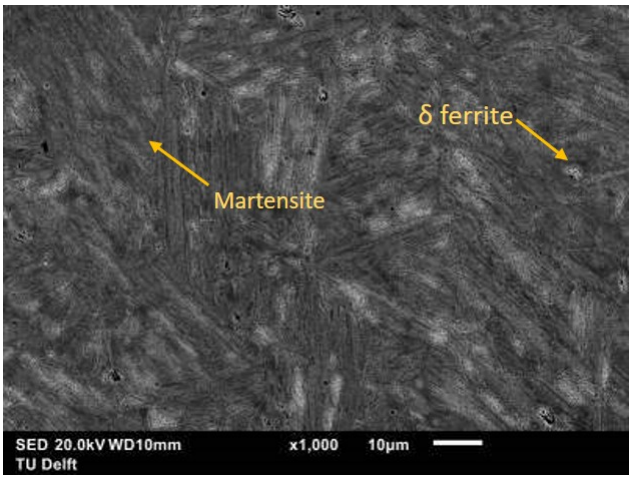

Figure 4.3: Microstructure of OC Weld Metal

4.1.5. Presence of Single Weld Bead Defects

The OC weld metal consisted of weld defects such as pores and worm holes as shown in *Figure 4.4*.

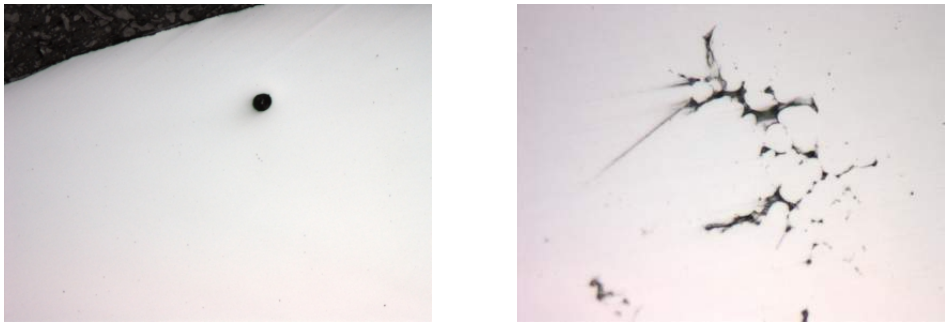

(a) Pores (b) Worm Holes

Figure 4.4: Defects in the Weld Metal

4.2. Optimal Condition (OC - R)

The results, findings and interesting findings of the optimised condition determined through the Ramping methodology is detailed in this section.

4.2.1. Input Parameters

The predicted and experimentally determined optimal condition is shown in *Table 4.3*. *Figure 4.5* shows the predicted optimal input and response parameters.

Table 4.3: Predicted and Experiment OC - R

Experiment			Predicted		
Current A	Voltage V	Travel Speed m/min	Current A	Voltage V	Travel Speed m/min
200	18.5	1.00	200	18.5	0.82

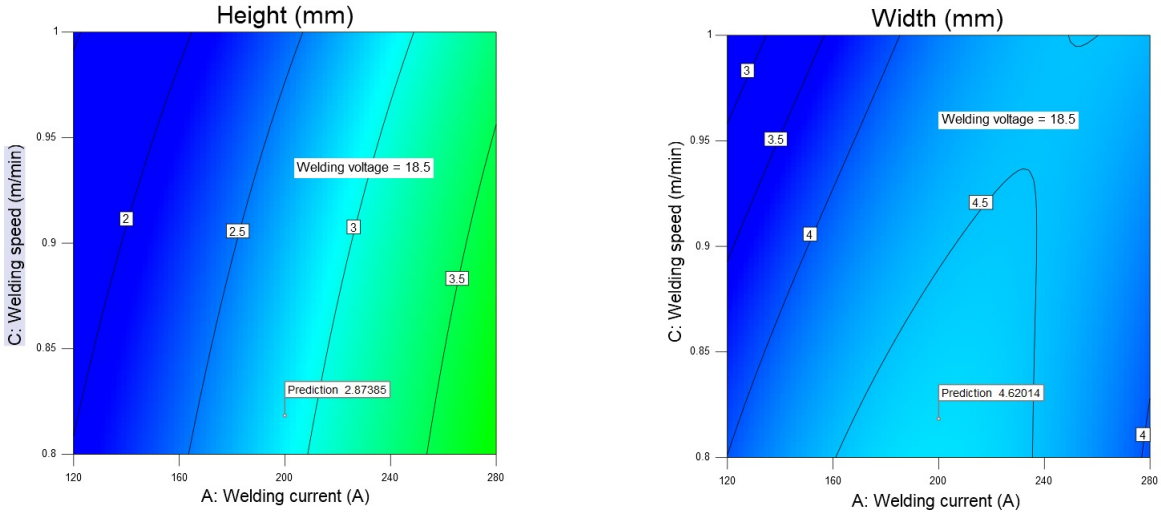

(a) Predicted Input and Height

(b) Predicted Input and Width

Figure 4.5: Predicted Input and Response parameters

4.2.2. Bead Parameters

After grinding and polishing the OC - R, bead cross - section was examined under an optical microscope as shown in *Figure 4.6*. The predicted and measured bead parameters are shown in *Table 4.4*.

Table 4.4: Measured Vs Predicted OC - R Bead Parameters

Measured			Predicted	
Width W (mm)	Height H (mm)	DoP mm	Width W (mm)	Height H (mm)
3.70	2.60	0.59	4.62	2.87

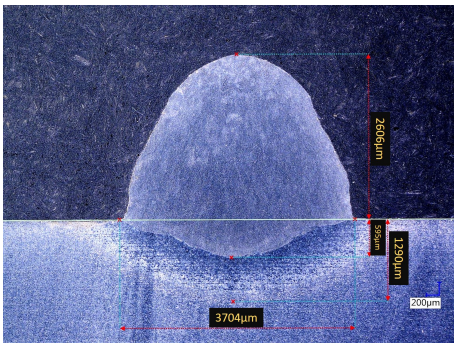

Figure 4.6: Optical Micrograph of OC - R Weld Metal

4.2.3. Hardness

The Vickers hardness test with 1kgf, 40x objective and 11 points of measurement across the weld bead resulted in a hardness value of 623 HV for the weld metal, 241 HV for the Heat Affected Zone (HAZ) and 186 HV for the substrate. The hardness profile is shown in *Figure 4.7*.

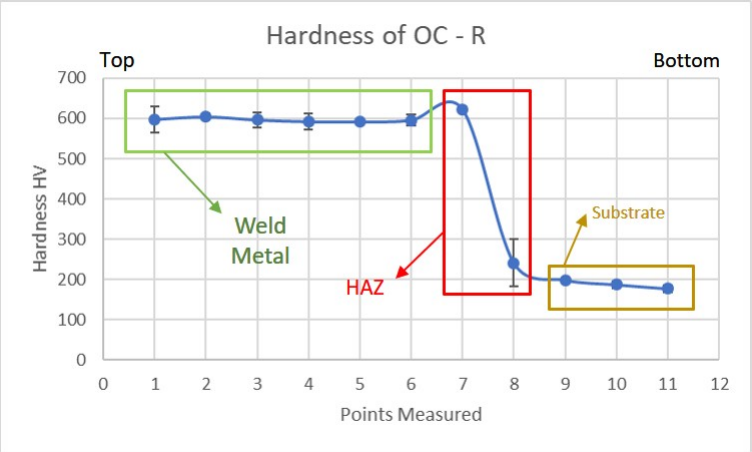

Figure 4.7: Hardness Profile of OC - R Weld Metal

4.2.4. Microstructure

The resulting microstructure consisted of δ-ferrite in the grain boundaries of a martensite matrix. At the fusion zone, the structure of the solidified δ-ferrite was in the form of cellular dendritic and at the top of the weld metal it was cellular equiaxed as shown in *Figure 4.8*.

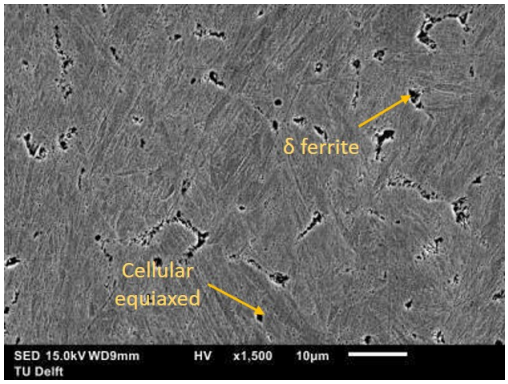

(a) Top

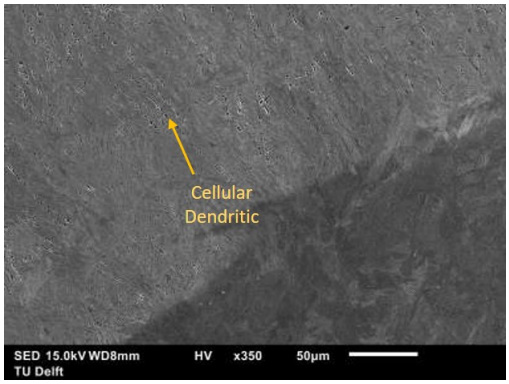

(b) Fusion Zone

Figure 4.8: Microstructure and Solidification Structures of OC - R

4.3. Comparison Between OC & OC - R

A comparison is presented in the *Table 4.5* to summarize how these conditions differ from each other.

Table 4.5: OC Vs OC - R

OC Vs OC - R Comparison		
Factors	**OC**	**OC - R**
Height of Bead (mm)	3.6	2.6
Width of Bead (mm)	9.9	3.7
Depth of Penetration (mm)	3.2	0.59
Preferred Overlap Ratio (mm)	6.6	2.5
W/H Ratio	2.75	1.42
Preheating	Yes, 200°C	Not required
Cooling	Air Cooled	Air Cooled
Presence of Defects	Pores, Worm Holes	None Observed
Spatter	Yes	No
Weld Quality	Smooth, No Color Shine	Smooth, Color Shine
Uniform Height	Yes	Yes
Uniform Width	Yes	Yes

Observing the comparison table above, it shows that the OC - R condition has advantages over the OC condition in terms of preheating, presence of defects, spatter and weld quality. Also, as previously mentioned the travel speed is 1.00 m/min and 0.59 m/min for OC - R and OC conditions respectively.

As preheating was not required for the deposition of the OC - R condition, it is advantageous in practical applications during the repair of defective moulds as no additional heat source is required. Eventually, it makes the process faster.

The OC - R condition had less spatter during deposition making a cleaner build and prevent contamination during overlapping. Lack of defects and a good surface quality of the weld will provide better machinability properties and end quality of the mould. The OC - R being faster in deposition is helpful to build large moulds in a shorter time and also quickly repair defective moulds.

From the above mentioned advantages of the OC - R condition, it is evident that this is more suitable for AM applications.

4.4. Additive Manufacturing with OC - R

This section details on the observations made during the additive manufacturing procedures.

4.4.1. Coating (or) Surface Cladding

1. Build Characterization:

   The build layer was flat on the surface with no visible imperfections. No presence of surface defects or spatter was observed on the as - built condition.

2. Defects:

   The clad was given to Villeroy & Boch to machine as per their industry standards. After machining 1 mm from the welded top surface, a small pore was found.

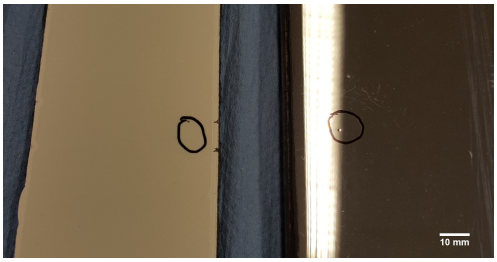

Figure 4.9: Pores on the surface

4.4.2. Wall Build - Oscillation Strategy

1. Build Characterization

   The resulting height of the build was 15 mm higher (65 mm) than what was modelled and programmed (50 mm).

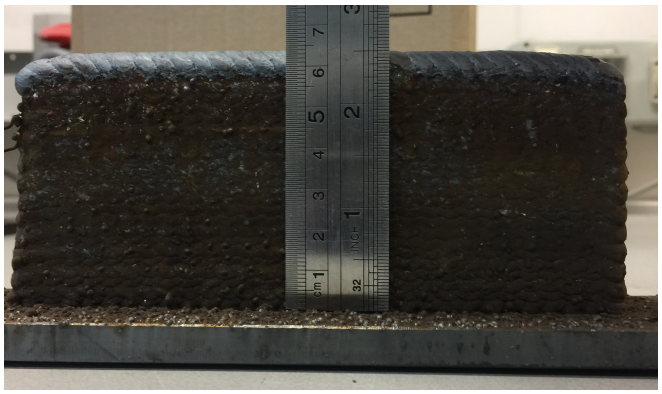

Figure 4.10: Overbuilt of Height

2. Randomly distributed pores:

   Presence of spatter was observed all around the substrate. Random occurrences of pores were also seen in the transverse and longitudinal cross - sections of the build.

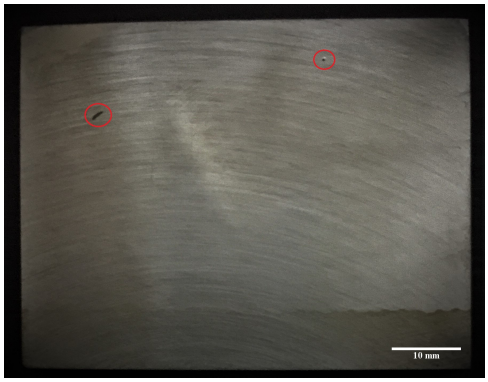

(a) Pores and inclusion in the longitudinal cut

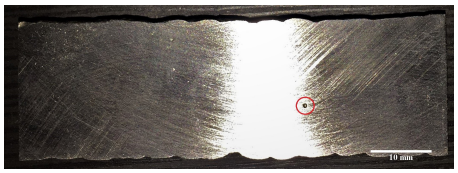

(b) Pore in the transverse cut

Figure 4.11: Defects in the Oscillation Strategy Wall Build

4.4.3. Wall Build - Straight line with alternative welding directions

1. Build Characterization:

   Similar to the oscillation strategy, the resulting height was also 15 mm than what was programmed.

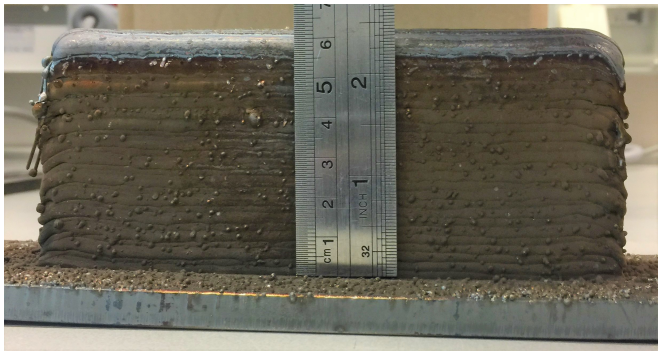

Figure 4.12: Overbuilt of Height

2. Randomly distributed pores:

   After initial transverse cuts on the extreme edges of the build, numerous pores were observed.

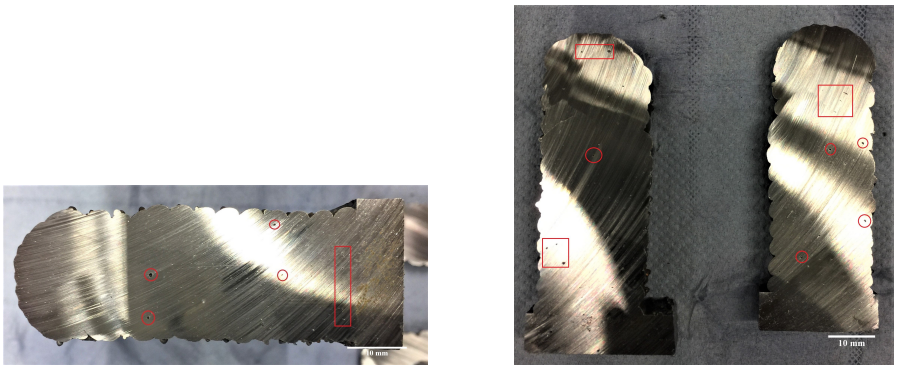

(a) Pores on the build

(b) Pores on the cut edges

Figure 4.13: Defects in the straight line with alternate welding direction wall build

5

Discussion

This chapter focuses on the discussion of the understanding and the results that were presented in *Chapter 4.*

5.1. Effect of Input Parameters on Weld Geometry

Firstly, the role or influence of the input parameters (Current, Voltage and Travel Speed) on the dependent variables (Height, Width and Depth of Penetration) is needed to be understood as to why they are optimal.

The influence of Current, Voltage and Travel Speed is explained and made understood in the paragraphs below:

1. Welding Current (Amps) [55]:

   From the *Figure 5.1* shown below, the cross - sections (1 - 5) is deposited with increase in amperage values from 100 - 250A with a constant voltage of 24V and a travel speed of 0.38 m/min. The current primarily controls the amount of weld metal that is deposited during welding. It also affects the weld penetration shown as a red outline. In beads 3 - 5, the mode of metal transfer was spray. The mode transitions from globular to spray at approximately 190A and above.

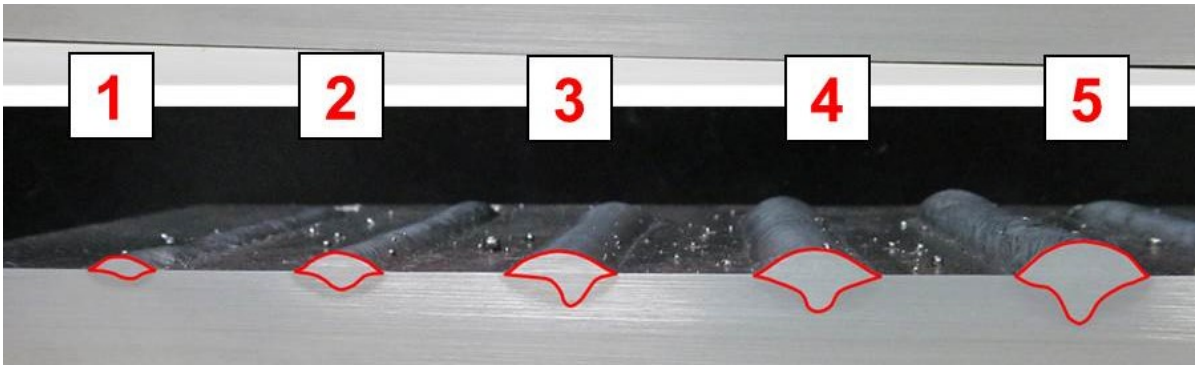

Figure 5.1: Effect of Current on Weld Bead Profile [55]

2. Welding Voltage (V) [55]:

   Figure 5.2 (a) below shows the influence of voltage on weld bead profiles. The beads 7 - 11 were welded with voltage values from 18 - 30V with a constant wire feed speed of 8 m/min and 0.38 m/min travel speed. The voltage controls the arc length [56] which is the distance between the molten weld pool and the metal wire at the point of melting in the arc (*Figure 5.2 (b)*). When the voltage is increased, the weld bead begins to flatten and has increasing width to depth ration. Here again the mode of transfer was changed from globular to spray at approximately 23V and above.

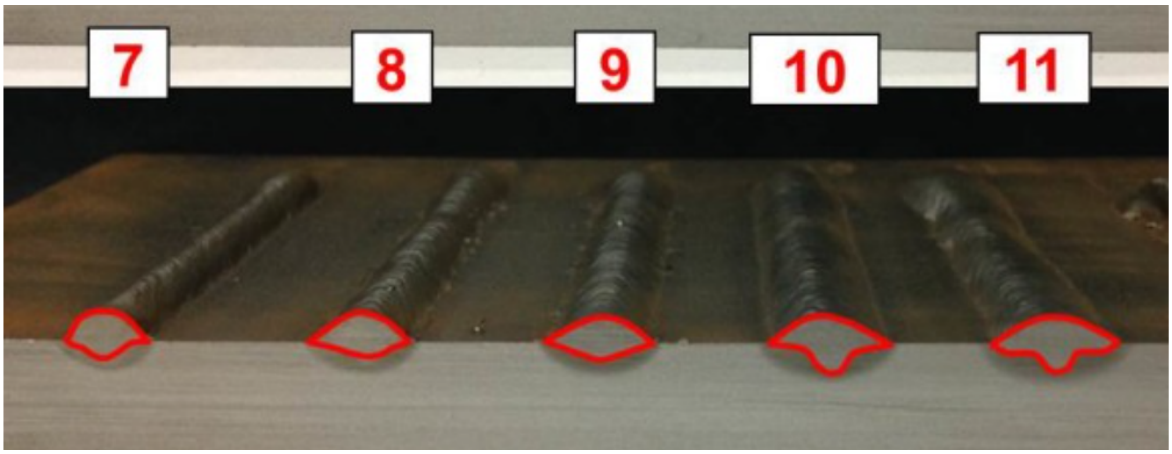

(a) Effect of Voltage of Weld Bead Profile

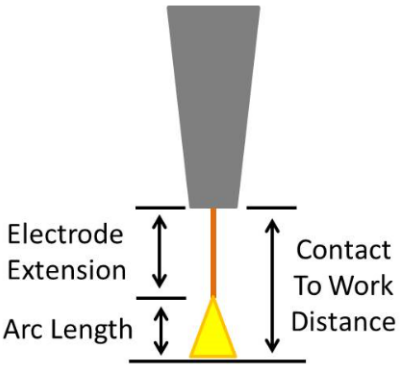

(b) Arc Length Schematic

Figure 5.2: Effect of Voltage on Weld Bead Profile [55]

3. Travel Speed (m/min) [57]:

   Travel speed on the other hand influences the DoP as shown in *Figure 5.3*. The physics behind is that at slower travel speeds, the arc is directly above the center of the weld pool and that the metal is transferred from the wire is directly deposited into the centre of the weld pool.

   In this case, the weld pool acts as a large cushion thereby reducing the penetration degree of the molten metal droplets on the base material. In faster travel speeds the vice versa happens and a deeper DoP is visualized.

   Travel speed also influence the solidification pattern of the resulting weld bead. From *Figure 5.3 (b)* it can be seen that at slower travel speeds, a circular or oval pattern results on the bead. At faster travel speeds, a V - shaped pattern is observed.

To summarise, in simpler terms, the current (amps) produces the heat and penetration, the voltage produces the arc that carries this heat and the travel speed supports this heat and the resulting molten metal to be deposited on the substrate.

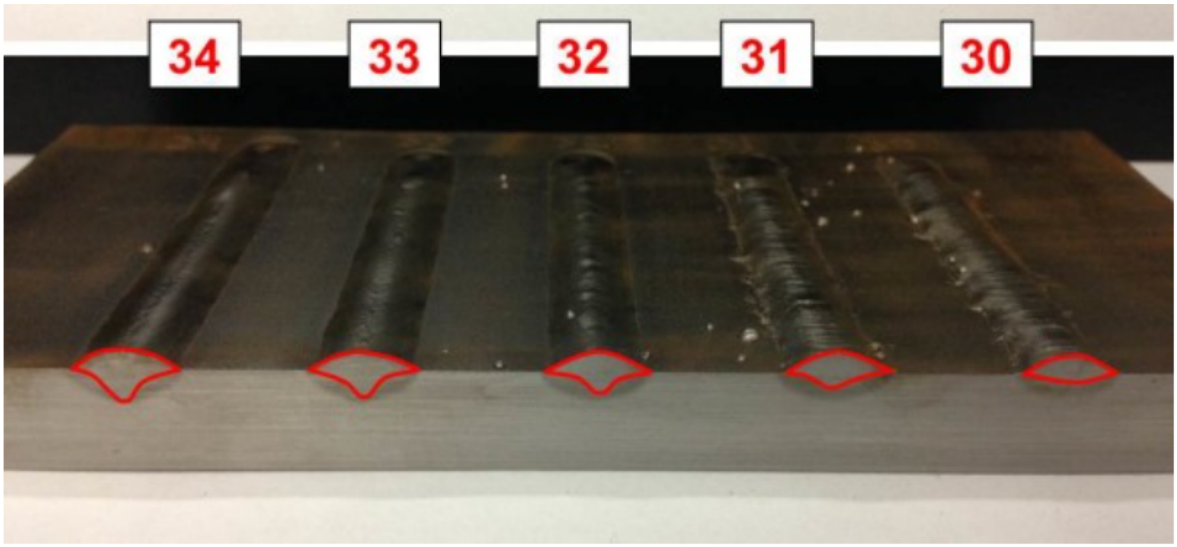

(a) Effect of Travel Speed on Weld Bead Profile

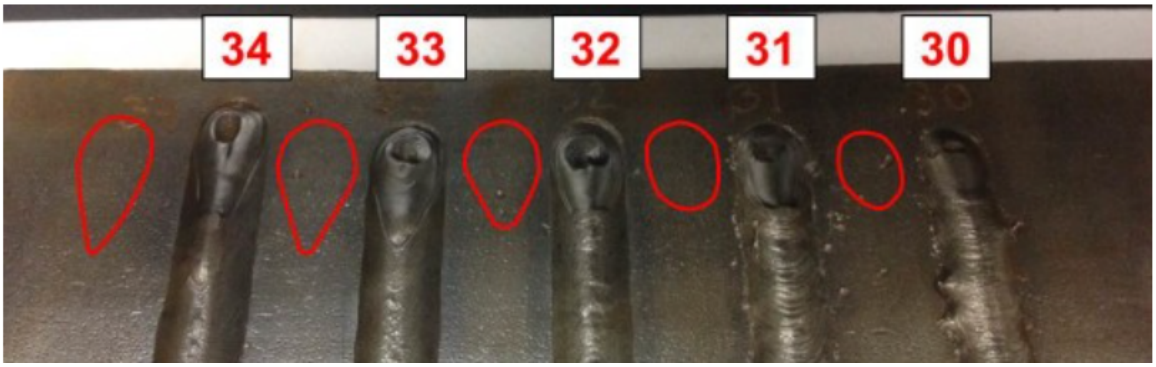

(b) Solidification Patterns

Figure 5.3: Effect of Travel Speed on Weld Bead Profile [57]

5.2. Optimal Condition (OC)

The trial data from *Table 3.4* was fed into Minitab for the conditions of maximum width, minimum height and minimum depth of penetration. Where the DoP is the main priority combined with less spatter evolution. Minitab was then able to optimize and obtain a proper combination of the input parameters that resulted in a weld bead shown in *Figures 3.6 & 3.7*.

Although RSM was able to provide with the OC conditions, the interaction between the input and response parameters is not clear. Therefore, the ramping experiments combined with RSM was carried out.

5.2.1. Defects

Some of the weld defects that were observed and their reasoning are detailed below.

1. Pores [58]:

   Pores can be formed due to many reasons and depending on size can be caused by different factors. One such factor is the presence of gas cavities that are trapped during welding. They are usually formed by the absorption of diatomic gases such as Nitrogen or Hydrogen from the surrounding atmosphere and not only from the shielding gases themselves.

   When the absorbed gas concentration exceeds the solubility limit, nucleation and growth of gas bubbles results in the liquid weld metal. These bubbles eventually become large and try to escape to the surface. Therefore, the pores are usually spherical in shape and in some cases long pores (or) worm holes may be formed.

   In the OC both pores and worm holes were observed and the formation of these pores can be attributed to the absorption of N_2 or H_2 from the atmosphere although none of these gases were used as a blend for the shielding gas. Another reasoning could be due to the formation of carbon monoxide gases resulting from the oxidation of carbon present in AISI 420.

   Other factors include presence of impurities from unclean substrate, spatter inclusion that remain during welding and contamination of welding wire.

2. Lack of Fusion [58]:

   This weld defect generally occurs when the liquid molten metal comes into contact with unmolten substrate. In simple terms, the energy or heat input was not high enough for the arc to melt the substrate.

   This results in insufficient bonding between the substrate and the weld metal. More commonly, lack of fusion can occur due to presence of oxides or other impurities that were not removed prior to welding.

5.3. Optimal Condition (OC - R)

This section is focused towards the Optimal Condition (OC - R) that was formulated and obtained using the parametric scanning procedure and RSM.

5.3.1. Effects of Input Parameters on Weld Width

1. Effect of Welding Current on Weld Width

   Figure 5.4 shows the effects of welding current on weld width for a constant welding speed of 0.6m/min and welding voltage of 20.2V. It is observed that the weld width increases and peaks at 200A and decreases as the weld current increases.

   This is due to the weld deposition efficiency is high until 200A and then reduces. Which means as the width reduces, the height increases and compensates for the volume to be constant. This is visualized in *Figure 5.8*.

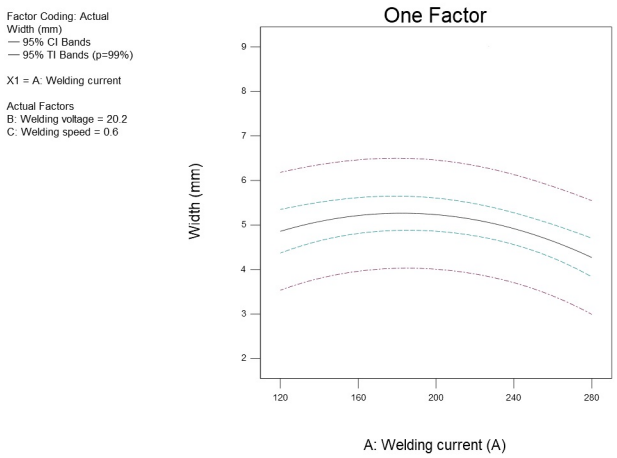

Figure 5.4: Effect of Welding Current on Weld Width

2. Effect of welding speed on weld width

Figure 5.5 shows the effect of welding speed on weld width for a constant welding current of 200A and welding voltage of 20.2V. It is observed that as the speed increases, the width decreases. The increased welding speeding reduces energy input leading to the reduction of the weld width [22].

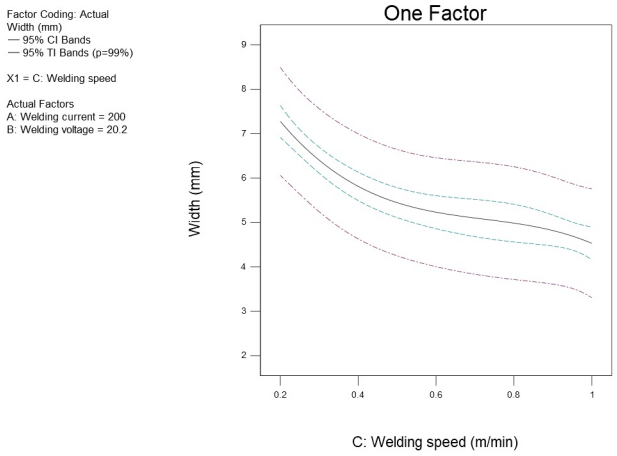

Figure 5.5: Effect of Welding Speed on Weld Width

3. Effect of welding voltage on weld width

Figure 5.6 shows the effect of voltage on weld width for a constant welding current of 200A and welding speed of 0.6m/min. It is observed that the weld width increases as the welding voltage. This is corresponding to the weld bead flattening effect by the arc which it was also mentioned earlier in *Section 5.1.1.*

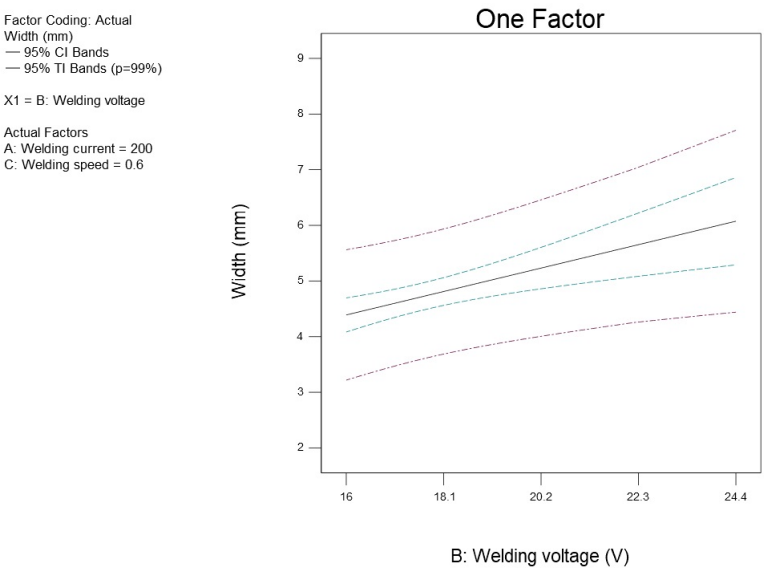

Figure 5.6: Effect of Welding Voltage on Weld Width

4. Effect of welding current and weld speed on weld width

Figure 5.7 shows the combined interactive effect of current and speed on weld width for a Constant voltage of 20.2V.

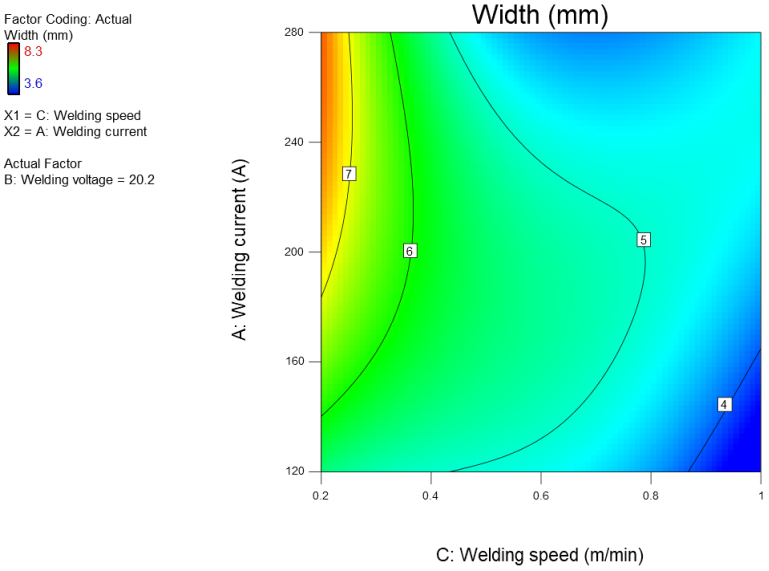

Figure 5.7: Effect of Welding Current & Speed on Weld Width

5.3.2. Effects of Input parameters on Weld Height

1. Effect of welding current on weld height

Figure 5.8 shows the relationship between current and weld height for a constant welding voltage of 20.2V and welding speed of 0.6m/min. It is observed that as the current increases, the height also increases. This is due to more metal being deposited with a higher energy input because of fixed feeding efficiency under 95%. Instead of metal spreading, it is more efficient in the increase in weld height.

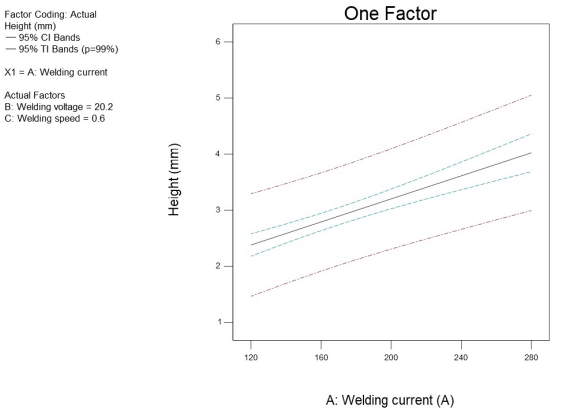

Figure 5.8: Effect of Welding Current on Weld Height

2. Effect of welding speed on weld height

Figure 5.9 shows the effect of welding speed on the weld height for a constant welding current of 200A and welding voltage of 20.2V. It is observed that the height decreases as the speed increases. This can be explained with the same reasoning as mentioned earlier which is due to the diminished interaction time of the wire and the molten weld pool.

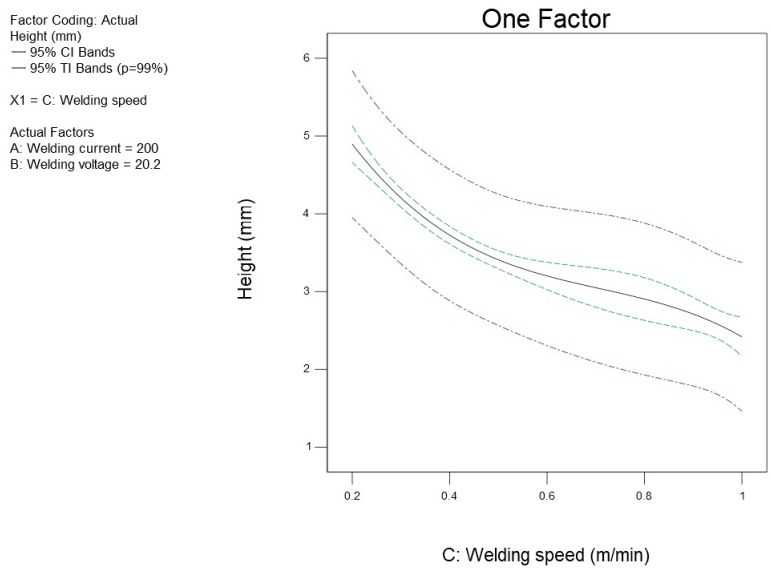

Figure 5.9: Effect of Welding Speed on Weld Height

3. Effect of welding current and welding speed on weld height

Figure 5.10 shows that combined interactive effect of current and weld speed for a constant voltage of 20.2V. Increased welding speed reduces the weld height. Increased welding current increases the weld height.

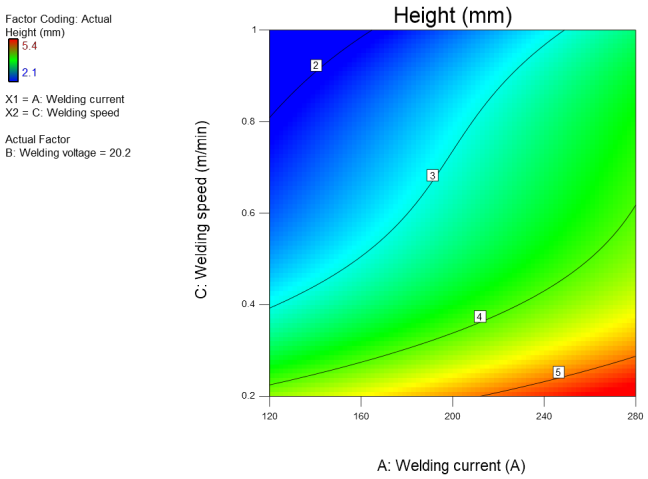

Figure 5.10: Effect of Welding Current & Speed on Weld Height

The effects mentioned above is shown in *Figure 5.11 (a) - (e)* from the bead cross sections of the bead shown in *Figure 3.12* which is tabulated in *Table 5.1* with increase in energy input. After the OC - R sample, DoP is increased and the height decreases. The requirement is to have minimum DoP and less spatter as mentioned earlier. Only the OC - R condition satisfies them both and termed as the optimal condition.

Table 5.1: Measured Bead Parameters

Sample No.	Current A	Voltage V	Travel Speed m/min	Energy Input J/mm	Width W,mm	Height H,mm	DoP mm
2	180	18.0	1.0	194.40	3.63	2.17	0.71
OC - R	200	18.5	1.0	222.00	3.70	2.60	0.59
3	220	19.3	1.0	254.76	3.61	2.52	0.63
4	240	20.8	1.0	299.52	5.16	2.33	1.09
5	280	24.4	1.0	409.92	6.71	2.37	1.37

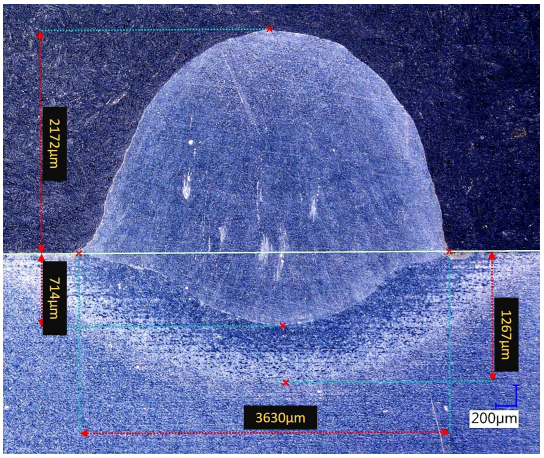

(a) 180A 18.0V 1.00m/min

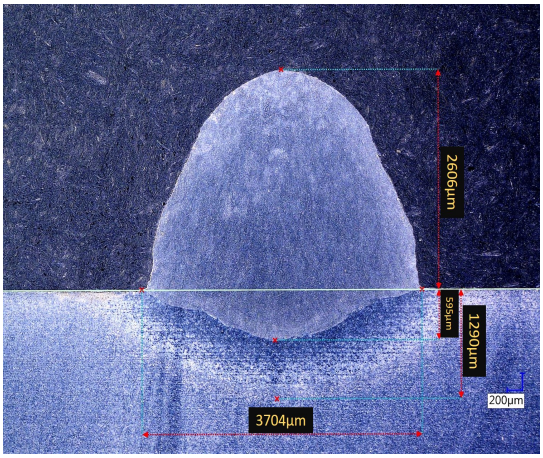

(b) 200A 18.5V 1.00m/min - OC - R

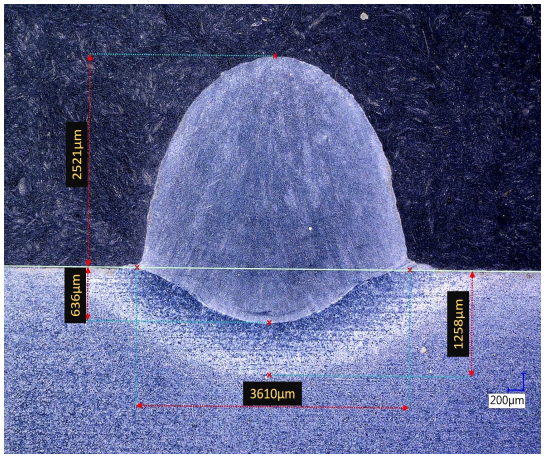

(c) 220A 19.3V 1.00m/min

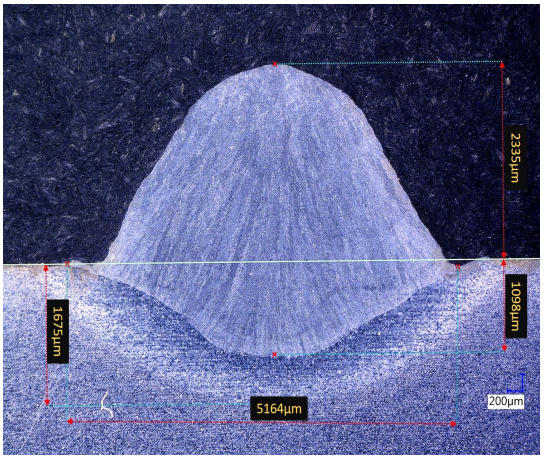

(d) 240A 20.8V 1.00m/min

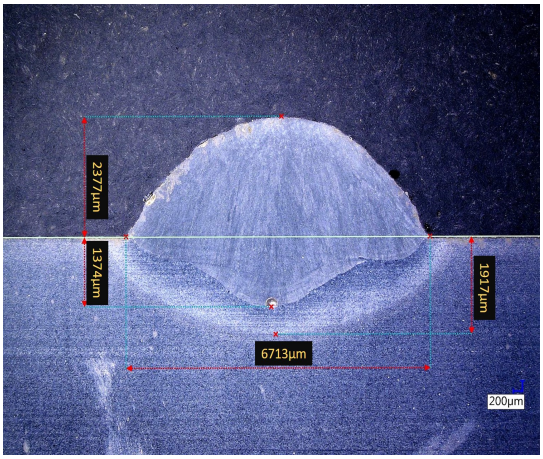

(e) 280A 24.4V 1.00m/min

Figure 5.11: Optical Microscope Images of the Ramping Samples

5.4. Microstructure Characterization

Microstructure characterization is performed to identify the resulting microstructure. Microstructure consists of phases that defines the material with its physical, mechanical and chemical properties. Different phases may be formed when the material is heated to liquid state and cooled down with different cooling rates. Depending on the steel alloy composition and cooling rate, during the solidification, different phases can be formed, such as Austenite, Martensite, Ferrite, etc,. The chemical composition of the alloy plays a major role in controlling as to which phases are formed.

Formation of phases can be understood or predicted using tools such as Phase Diagrams. These diagrams represent which phases are present at a temperature and concentration of the alloy. The chemical composition (wt.%) recalling from section 3.1 is shown in *Table 5.2* based on which the microstructure of as welded AISI 420 martensitic stainless steel is characterised. Based on the Carbon (0.38%) and Chromium (16%) composition, the isopleth of the Fe-Cr-C ortho-equilibrium phase diagram is calculated from Thermo-Calc and is shown in *Figure 5.12*.

Table 5.2: Chemical Composition of wire used wt.%

Material	C	Cr	Fe	Mn	Mo	Ni	Si
AISI 420	0.38	16	80.77	0.65	1.0	0.8	0.4

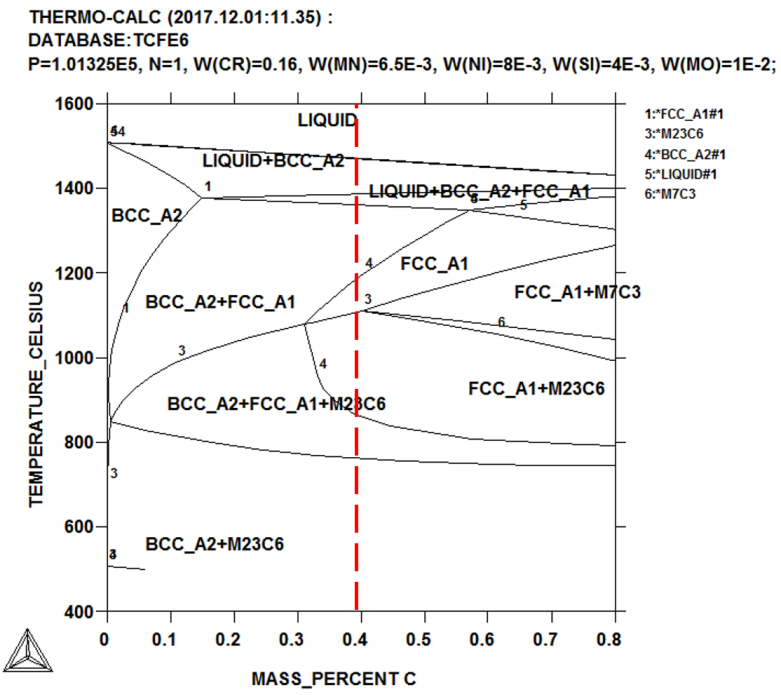

Figure 5.12: Isopleth of the Fe-Cr-C ortho-equilibrium phase diagram

AISI 420 has 0.38 wt.% C and when this material is welded with the OC – R weld conditions, the heat input is 222 J/mm and at this heat, temperature rises and the metal liquefies. The liquid weld metal then cools down and solidifies (red dashed line). The path that the weld metal follows during cooling determines it's resulting microstructural characteristics. At 1600°C, the metal is in the liquid phase (Liquid). At approximately 1500°C, the metal enters the liquid + δ-ferrite phase (`BCC_A2`). At 1400°C, the metal enters the liquid + δ-ferrite + γ-austenite phase (`FCC_A1`) and as the temperature reduces, the liquid phase transforms into solid and becomes fully austenitic at approximately 1300°C. Cooling down further, carbides ($M_{23}C_6$) begin to precipitate. This occurs when Chromium and Carbon begins to react with the ambient atmosphere and

are drawn out of the metal. Moving down further the red line, δ-ferrite + γ-austenite + $M_{23}C_6$ is formed and finally at approximately 820°C, δ-ferrite + γ-austenite transforms forming δ-ferrite (BCC_A2) + $M_{23}C_6$ phase as it cools down.

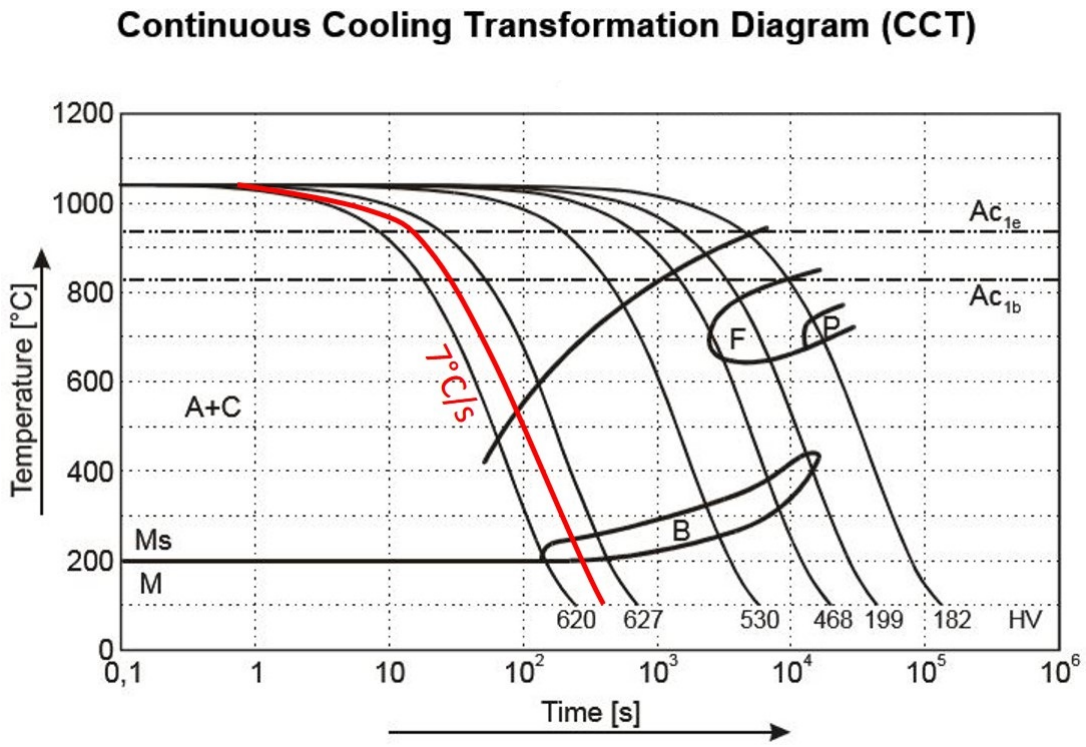

Figure 5.13: Continuous Cooling Transformation Diagram [59]

The continuous cooling transformation (CCT) diagram provides information on the phases formed at different cooling rates. *Figure 5.13* shown above is the CCT diagram for Type 420 stainless steel. From the thermocouple data for the OC - R condition, it is seen that the cooling rate is approximately 7°C/s. At this rate, the CCT indicates the formation of martensite at room temperature.

The following paragraphs describe the study done on the microstructure characterization of as-welded AISI 420 martensitic steel with reference to the phase diagram, CCT, literature references and eventually establishing a relationship with the process parameters.

The SEM micrographs of the ramping samples (2-5), OC - R and OC are shown in *Figure 5.17*. Observing the micrographs, white boundary like features is present in the grain boundaries. These features are also present in some surrounding phase matrix. They also seem to disappear as the heat input increases. Identification of these features and the surrounding phase matrix is elaborated in the following paragraphs.

From literature studies, the results and observations found by Kangda Hao et al.[60] on the "Effect of heat input on weld microstructure and toughness of laser-arc hybrid welding of martensitic stainless steel" seemed to have similar microstructural characteristics who reported the formation of δ-ferrite (BCC_A2) + martensite + $M_{23}C_6$ in the as - welded condition. They performed hybrid welding using the Type 420 martensitic stainless steel as the base material and ER310 wire as filler. Their weld metal consisted of two separate regions – Arc Zone (ArcZ) and Laser Zone (LaserZ). The ArcZ's SEM micrograph showed presence of martensite, austenite and δ-ferrite. This is similar to the microstructure that was evolved in the parametric scanning ramping sample (OC - R) with 180A, 18V and 1.00m/min SEM micrograph. The two micrographs are shown below for comparison.

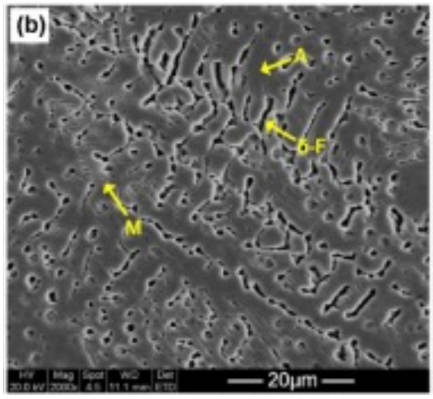

(a) ArcZ composed of austenite, martensite and δ-ferrite [60]

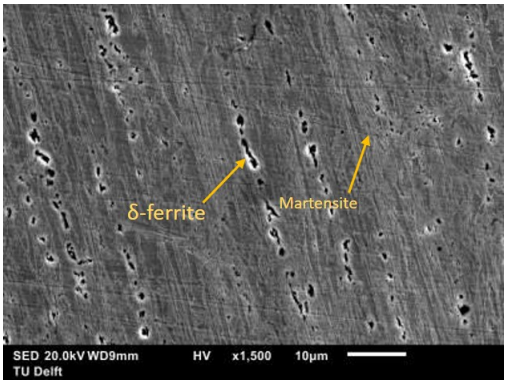

(b) SEM micrograph with 180A, 18.0V and 1.00m/min (OC - R)

Figure 5.14: Kangda's SEM compared to OC - R's SEM

Observations from other researches such as S.H.C Park et. al [61] reported that the δ-ferrite was formed along grain boundaries in an austenite matrix during friction stir welding. They suggested that during phase transformations of austenite to δ-ferrite, the δ-ferrite retained due to rapid cooling. Taban et. al [62] also observed formation of δ-ferrite at grain boundaries during laser welding of 12%Cr stainless steel. They reported that if the material cools fastly and reaches 1050°C within 1-2s, reversion of γ-austenite will not occur and δ-ferrite structure is maintained at the room temperature.

Folkhard et.al [63] stated that during solidification of martensitic stainless steels, new grain boundaries are formed which are mainly cellular or globular in structure. They also stated that alloys with high chromium and low nickel contents possess a high degree of δ-ferrite. Therefore, the white features is characterized to be δ-ferrite in reference to the studies mentioned above.

Krakhmalev et. al [64] performed Selective Laser Melting (SLM) on 420 grade stainless steel. They reported unusual amounts of austenite in their microstructural analyses. Their findings indicate deviation from the CCT diagram of 420 stainless steel. This makes our findings promising to be martensite. Also, the hardness values obtained from the OC - R sample indicate the cooling rate for which martensite is obtained in the room temperature. Therefore, the phase matrix is characterized to be martensite.

The martensite that is formed is transformed from austenite if cooling is rapid enough. This indicates that diffusional separation of carbon and iron is no longer possible. This diffusion - less transformation takes place at approximately below 200°C (M_s) as shown in *Figure 5.13*. The growth of martensite is considered athermal because while remaining at the same temperature the transformation does not proceed. The fraction of austenite being transformed depends on the temperature to which it is cooled. The martensite formed is therefore an interstitial supersaturated solid solution of carbon in iron having a body centered tetragonal lattice [59].

So, the relationship between the process parameters and the resulting microstructure can be explained as follows. At the heat input of 222 J/mm (OC -R), the cooling is fast enough for some fraction of austenite to transform into martensite while some δ-ferrite (white boundary) retains in the grain boundaries due to rapid cooling. As the heat input increases to 770 J/mm, the cooling rate slows down and seems to provide enough time for δ-ferrite to completely transform into marteniste at the room temperatures. There is a possibility to form retained austenite but it was not observe in this analyses.

The evloved microstructure does in fact comply with the requirements of the mould. To evaluate its machinability, the clad sample was sent to Villeroy & Boch but for some unknown reason they refused to provide their machinability report. However, the microstructure did not hinder the hardness property of the weld as they were well within the required range.

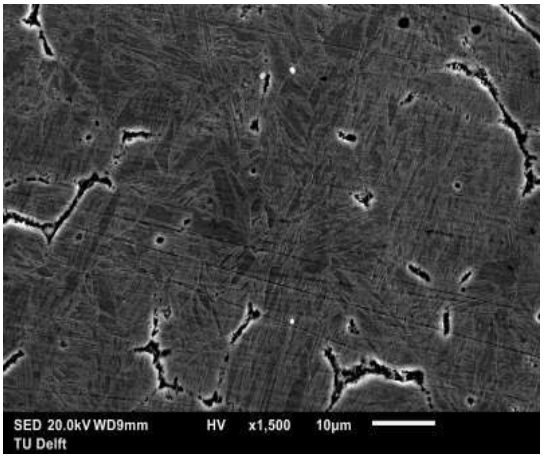

(a) 180A 18.0V 1.00m/min

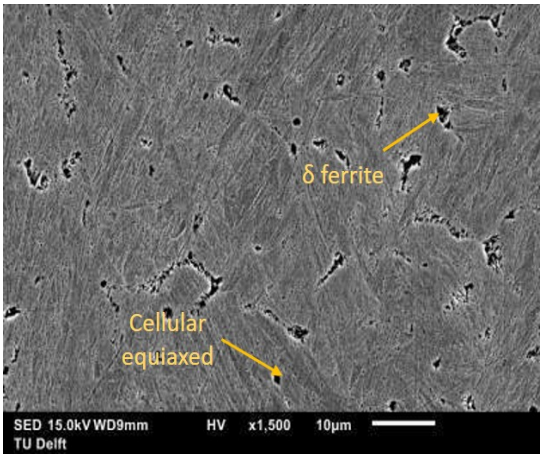

(b) 200A 18.5V 1.00m/min - OC - R

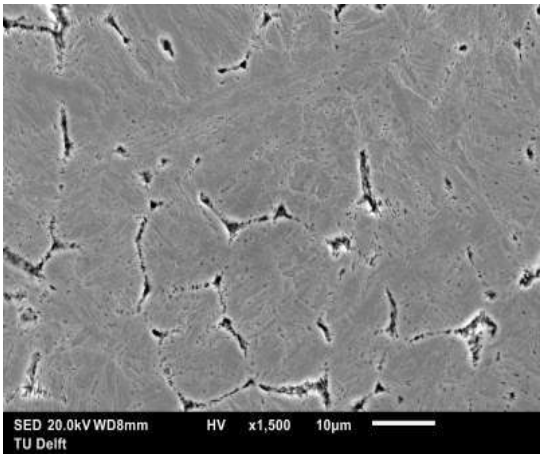

(c) 220A 19.3V 1.00m/min

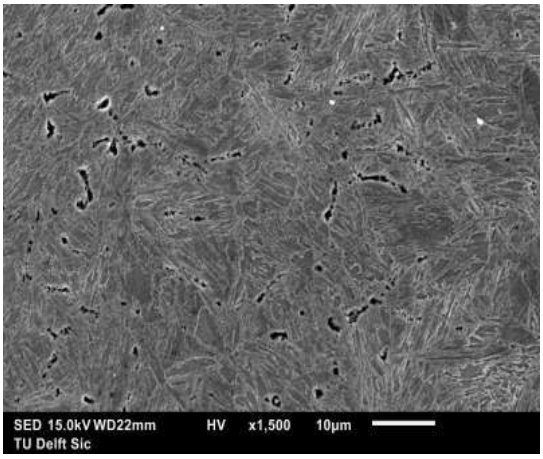

(d) 240A 20.8V 1.00m/min

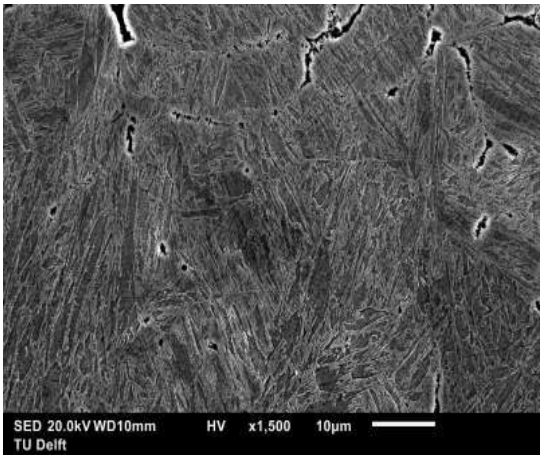

(e) 280A 24.4V 1.00m/min

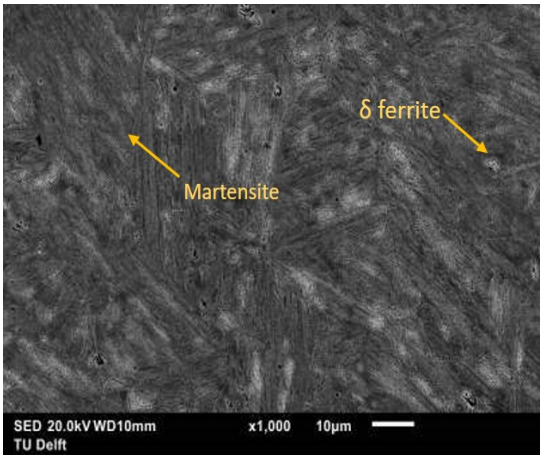

(f) 261A 29V 0.59m/min - OC

Figure 5.15: SEM Micrographs of the Ramping Samples, OC - R and OC

5.4.1. Solidification Structures

The solidification structures formed in the ramping samples were cellular dendritic at the fusion zone and cellular equiaxed at the top of the weld bead as shown in *Figure 4.8*. This is due to the effects of temperature gradient (G) and the solid - liquid interface growth rate (R) which was explained earlier in *Section 2.3*. The mode of solidification is controlled by the the G/R ratio and (G.R) controls the scale of these structures. An unstable planar growth proceeded to break down into dendrites within short distances from the fusion zone thereby they formed the majority of the solidification microstructure. The dendritic to equiaxed transition takes place when the nucleation of equiaxed grains occurs in the liquid ahead of the dendritic structure.

5.4.2. Cracks

Either in the single weld bead or the multi - layered wall build, no cracks either cold or hot cracks were detected. This is due to the presence of δ-ferrite in the microstructure. V Shankar et. al [27] claims that even a few percent (5 - 35%) of δ-ferrite gives the metal it's crack resistance properties. As mentioned earlier impurities such as sulphur and phosphorous promotes cracking leading to the fact that there were no such impurities in the weld metal. Also, Abdel et. al [65] stated that presence of mixed solidification structures results in a crack free weld.

5.5. Hardness Analysis

As mentioned earlier in *Section 2.4*, the Carbon content determines the hardness of the material. *Figure 5.16* shows the microhardness profile [24] across different regions of the weld which is similar to the hardness profile shown in *Chapter 4*. Observing the *Figure 4.7* in *Section 4.2.3*, the drop in hardness in the HAZ is due to the presence of softer δ-ferrite phase situated at the martensite grain boundaries. The highest hardness in the HAZ is due to carbon is in supersaturation in the martensitic lattice instead of precipitating in the form of carbides, thus contributing to the hardness of the martensite. Moving across, it is seen that the hardness reduces even further due to incomplete dissolution of carbides at lower austenization temperatures. The hardness in the substrate results from over tempering which is reheating and cooling thereby reducing the hardness in the microstructure of the substrate. The hardness values of both OC (514HV) and OC - R (623HV) seemed to satisfy the requirement for machinability of moulds as mentioned earlier in *Chapter 1, Section 1.3*. It was also observed that the hardness reduces with increase in heat input.

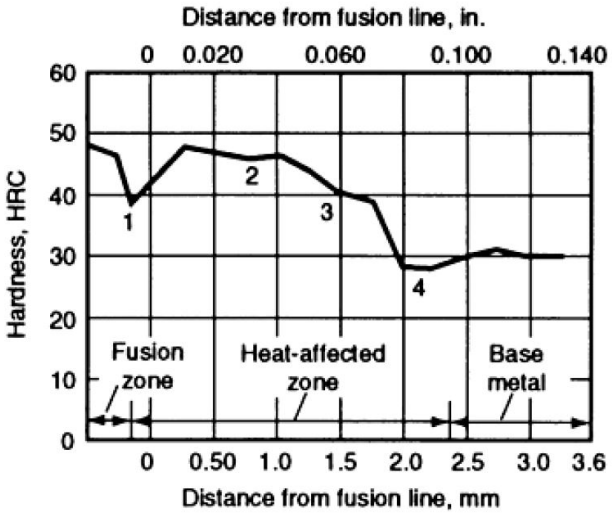

Figure 5.16: Microhardness Profile [24]

5.6. Additive Manufacturing

This section explains the observations made with the build samples - Oscillation and Solid Part Strategy.

5.6.1. Oscillation Part Strategy

This strategy has significant better build quality results when compared to the solid part strategy. This could be due to the toolpath configuration where in the robot follows a zig-zag path that produces a weld that is perfectly overlapped resulting in a smooth build profile.

1. Defects:

   Some random pores were seen when the build was examined for it's transverse and longitudinal cross - sections. These pores can be attributed to the explanation given in the previous section as to the absorption of di - atomic gases. These pores can be prevented if proper amount of shielding gas is supplied to the work piece so that it can restrict the influx of these gases.

2. Overbuild of Height:

   The strategy was programmed to build a wall of 50mm in height but, the resulting build had a height of 65mm. This can be explained due to the fact that while welding, the height of the first layer was not 2.60mm. This means that the overlap ratio was too small and thus affecting the step - up value as well.

5.6.2. Straight Line with Alternating Weld Directions

This strategy's resulting build had a good surface quality from the outside until it was cut in the traverse direction where numerous pores were observed.

1. Defects:

   The numerous pores that were observed more in this strategy can be reasoned out due to the increase in entrapment and solubility of the di - atomic gases in the build.

2. Overbuild of Height:

   In this strategy, the step up value was not properly calculated and set resulting in the overbuild.

5.7. Summary

Role of input parameters (Current, Voltage and Travel Speed) on the response parameters (Width, Height and DoP) were discussed. The effects of the input parameters for RSM (OC) was not clear so further investigation was performed through parametric scanning. Defects on the (OC) weld beads and their causes were also discussed.

With parametric scanning ramping samples (OC - R), relationship between the input and response parameters were established and discussed.

Further microstructure characterization was perfomed using SEM analyses which revealed presence of δ-ferrite at the grain boundaries of martensite matrix. The δ-ferrite seemed to reduce as the heat input increased. Hardness analysis on the OC and OC - R samples were discussed on their respective hardness values.

Finally, additive manufacturing with the OC - R condition and its build characteristics were also discussed.

6

Conclusions and Recommendations

6.1. Conclusions

The aims of this research mentioned in *Chapter 1, Section 1.4* was accomplished by the following:

1. Statistical models were developed to navigate in the range of input parameters and define it's optimal input conditions.
2. Resulting weld beads were inspected for their quality.
3. Microstructure was characterized using optical microscopy and SEM analysis.
4. Hardness values were determined and related to the input parameters.
5. Moreover, additive manufacturing was performed by building walls with different toolpath strategies.

The conclusions obtained from the above are elaborated as follows:

1. Statistical Model
   - RSM and parametric scanning was performed to optimize the input parameters.
   - The optimal condition from RSM was 261A, 29V and 0.59m/min (OC).
   - The optimal condition from parametric scanning combined with RSM was 200A, 18.5V and 1.00m/min (OC - R).
   - The model was also used to understand the influence of the input parameters on the response parameters.
   - It was found that as the travel speed increases, the width and the height decreases.
   - As the current increases, the width increases to a point and then decreases while the height increases.
   - As the voltage increases so does the width. But it has no effect on the height.
2. Weld Bead Quality
   - Weld bead from OC consisted of pores and worm holes in the weld metal. More spatters were also observed.
   - Weld bead from OC - R did not possess any defect nor spatters.
3. Microstructure
   - It was observed that the as - welded microstructure consisted of δ-ferrite in a martensite matrix.
   - The δ-ferrite solidified in the form of cellular dendritic structure in the fusion zone and cellular equiaxed at the top of the weld metal.

- The concentration of δ-ferrite reduces as heat input increases.

4. Hardness
   - The Vickers hardness of the OC weld metal was ±514HV.
   - The Vickers hardness of the OC - R weld metal was ±623HV.
   - The hardness values obtained were attributed to the amount of carbon present and carbide dissolution.
   - Hardness reduced with increase in heat input.
5. Additive Manufacturing
   - The OC weld metal was found to be not suitable for AM applications due to presence of pores and non uniform surface.
   - Therefore the additive manufacturing was performed with the OC - R welding conditions.
   - Autodesk Powermill was used to program toolpaths for the oscillation and straight line with alternate welding direction strategy.
   - Cross sectional analysis of the oscillation strategy showed very good and acceptable levels of build quality as per industry standards although pores were seen at the top of the build.
   - Cross sectional analysis of the straight line strategy showed numerous pores making the build unacceptable.

6.2. Recommendations

Some recommendations to further improve the results obtained in this research are mentioned as follows:

1. Although many statistical models were proposed to optimize the input parameters only RSM and parametric scanning were used in this research. Artificial Neural Network (ANN) together with other statistical models may provide better optimization results.
2. The shielding gas in itself can be altered and studied on it influence on the response parameters and the build quality.
3. A substrate with a similar chemical composition as the welding wire can be made use of to obtain better weld profiles and resulting microstructure.
4. Post weld heat treatment can be employed to better determine and characterize the required microstructure of the weld metal.
5. The step over and step up variables while performing additive manufacturing can be better optimized with the use of powerful CAD simulations.

Bibliography

[1] Ian Gibson, David W Rosen, Brent Stucker, et al. *Additive manufacturing technologies*, volume 238. Springer, 2010.

[2] Dongming Hu and Radovan Kovacevic. Sensing, modeling and control for laser-based additive manufacturing. *International Journal of Machine Tools and Manufacture*, 43(1):51–60, 2003.

[3] David L Bourell, Ming C Leu, and David W Rosen. Roadmap for additive manufacturing: identifying the future of freeform processing. *The University of Texas at Austin, Austin, TX*, pages 11–15, 2009.

[4] Super Fast 3D Printer for Huge Objects. URL https://www.fastcodesign.com/3058289/autodesk-built-a-super-fast-modular-3-d-printer-for-huge-objects.

[5] 3D Printing Vs Traditional Manufacturing. URL https://www.marlinwire.com/blog/3d-printing-vs-traditional-manufacturing.

[6] Ian Gibson, David Rosen, and Brent Stucker. *Directed Energy Deposition Processes*, pages 245–268. Springer New York, New York, NY, 2015. ISBN 978-1-4939-2113-3. doi: 10.1007/978-1-4939-2113-3_10. URL https://doi.org/10.1007/978-1-4939-2113-3_10.

[7] Types of 3D Printing Technologies. URL http://3dprintingfromscratch.com/common/types-of-3d-printers-or-3d-printing-technologies-overview/.

[8] Bishal Silwal Michael Santangelo, Alex Purdy. Wire + arc additive manufacturing.

[9] N Pépe, S Egerland, P A Colegrove, D Yapp, A Leonhartsberger, and A Scotti. Measuring the process efficiency of controlled gas metal arc welding processes. *Science and Technology of Welding and Joining*, 16(5):412–417, 2011. doi: 10.1179/1362171810Y.0000000029. URL https://doi.org/10.1179/1362171810Y.0000000029.

[10] Tips for Designing 3D Printed Parts. URL https://innovationstation.utexas.edu/tip-design/.

[11] AS Schulz-Beenken. Martensite in steels: its significance, recent developments and trends. *Le Journal de Physique IV*, 7(C5):C5–359, 1997.

[12] Arcelor Mittal. Steel solutions for plastic moulding. URL http://industeel.arcelormittal.com/wp-content/uploads/2016/01/INDUSTEEL_Steel-Molds-tools-die.pdf.

[13] Iron Foundry. Reasonable machining hardness range for iron and steel castings. URL http://www.iron-foundry.com/machining-hardness-range.html.

[14] Strength Examining Mold Hardness. URL http://www.afsinc.org/about/content.cfm?ItemNumber=10450.

[15] Wikipedia. Tool steels. URL https://en.wikipedia.org/wiki/Tool_steel.

[16] Surgical Stainless Steel. URL https://en.wikipedia.org/wiki/Surgical_stainless_steel.

[17] Villeroy and Boch Wellness. URL https://www.villeroy-boch.de/bad-und-wellness/inspiration.html.

[18] KY Benyounis and AG Olabi. Optimization of different welding processes using statistical and numerical approaches–a reference guide. *Advances in engineering software*, 39(6):483 – 496, 2008.

[19] I.S Kim, J.S Son, I.G Kim, J.Y Kim, and O.S Kim. A study on relationship between process variables and bead penetration for robotic co2 arc welding. *Journal of Materials Processing Technology*, 136(1): 139 – 145, 2003. ISSN 0924-0136. doi: https://doi.org/10.1016/S0924-0136(02)01126-3. URL http://www.sciencedirect.com/science/article/pii/S0924013602011263.

[20] N Murugan and R.S. Parmar. Effects of mig process parameters on the geometry of the bead in the automatic surfacing of stainless steel. 41:381–398, 03 1994.

[21] V Gunaraj and N Murugan. Application of response surface methodology for predicting weld bead quality in submerged arc welding of pipes. *Journal of Materials Processing Technology*, 88(1):266 – 275, 1999. ISSN 0924-0136. doi: https://doi.org/10.1016/S0924-0136(98)00405-1. URL http://www.sciencedirect.com/science/article/pii/S0924013698004051.

[22] Wei Ya. *Laser Materials Interaction During Cladding - Analyses on Clad Formation, Thermal Cycles, Residual Stress and Defects*. PhD thesis, 2015.

[23] Pierre-Juan Cunat. *The Welding of Stainless Steels*, volume 3. 2007.

[24] ASM Handbook. *Welding, Brazing and Soldering ASM Handbook*.

[25] Dr. G. Balachandran. Stainless steel processing to meet advanced applications. URL http://www.stainlessindia.org/UploadPdf/.Basics%20of%20Stainless%20Steel%20Making%20&%20its%20Physical%20Metallurgy.pdf.

[26] A. Balogh L. Beres and W. Irmer. Welding of martensitic creep - resistant steels. *Supplement to the Welding Journal*, pages 191 – 195, 2001.

[27] V Shankar, TPS Gill, SL Mannan, and S Sundaresan. Solidification cracking in austenitic stainless steel welds. *Sadhana*, 28(3-4):359–382, 2003.

[28] DJ Widgery. Effects of sulphur and phosphorous on weld-metal solidification cracking. *Metal Constr Brit Weld J*, 2(8):333–338, 1970.

[29] Nickel Development Institute. *Welding of Stainless Steels and Other Joining Methods*, volume 9002. 1988.

[30] Damian Kotecki and Frank Armao. *Stainless Steels Welding Guide*. 2003.

[31] TG Gooch. Heat treatment of welded 13% cr-4% ni martensitic stainless steels for sour service. *Welding Journal-Including Welding Research Supplement*, 74(7):213s, 1995.

[32] Ceyhun Köse and Ramazan Kaçar. The effect of preheat and post weld heat treatment on the laser weldability of aisi 420 martensitic stainless steel. *Materials and Design*, 64:221 – 226, 2014. ISSN 0261-3069. doi: https://doi.org/10.1016/j.matdes.2014.07.044. URL http://www.sciencedirect.com/science/article/pii/S0261306914005767.

[33] Mirrax ESR. *Assab*. 080828 edition, 2008.

[34] Mehmet Erdem, Mehmet Altuğ, and Mustafa Karabulut. Investigation of mechanical, microstructural, and machining properties of aisi 420 martensitic stainless steel welded by laser welding. *The International Journal of Advanced Manufacturing Technology*, 85(1):481–492, 2016. ISSN 1433-3015. doi: 10.1007/s00170-015-7924-2. URL http://dx.doi.org/10.1007/s00170-015-7924-2.

[35] R. K. Garg, K. K. Singh, Anish Sachdeva, Vishal S. Sharma, Kuldeep Ojha, and Sharanjit Singh. Review of research work in sinking edm and wedm on metal matrix composite materials. *The International Journal of Advanced Manufacturing Technology*, 50(5):611–624, 2010. ISSN 1433-3015. doi: 10.1007/s00170-010-2534-5. URL http://dx.doi.org/10.1007/s00170-010-2534-5.

[36] Aqueel Shah, Nadeem A. Mufti, Dinesh Rakwal, and Eberhard Bamberg. Material removal rate, kerf, and surface roughness of tungsten carbide machined with wire electrical discharge machining. *Journal of Materials Engineering and Performance*, 20(1):71–76, 2011. ISSN 1544-1024. doi: 10.1007/s11665-010-9644-y. URL http://dx.doi.org/10.1007/s11665-010-9644-y.

[37] Carpenter Speciality Alloys. *Guide to Machining Carpenter Speciality Alloys*.

[38] Ismail Hemmati, V Ocelík, and J Th. M. De Hosson. Microstructural characterization of aisi 431 martensitic stainless steel laser-deposited coatings. 46:3405–3414, 05 2011.

[39] Lilian Debra Barlow et al. *The effect of austenitising and tempering parameters on the microstructure and hardness of martensitic stainless steel AISI 420.* PhD thesis, University of Pretoria, 2010.

[40] ES Labortory. Etchant store. URL http://www.etchantstore.com/Kallings-2-Reagent-500-mL-154.htm.

[41] Todd A. Christman Katharine B. Small, David A. Englehart. Guide to etching speciality alloys. URL https://www.researchgate.net/file.PostFileLoader.html?id=558c52c860614be1d98b4588&assetKey=AS%3A273802167029766%401442290932019.

[42] A Turnbull and A Griffiths. *Corrosion and Cracking of Weldable 13 Cr Martensitic Stainless Steels: A Review.* National Physical Laboratory, 2002.

[43] Joseph R Davis et al. *Stainless steels.* ASM international, 1994.

[44] MOHD Shoeb, M Parvez, and P Kumari. Effect of mig welding input process parameters on weld bead geometry on hsla steel. *Int. J. Eng. Sci. Technol*, 5(1):200–212, 2013.

[45] Memduh Kurtulmus, Ahmet Irfan Yukler, Mustafa Kemal Bilici, and Zarif Catalgol. Effects of welding current and arc voltage on fcaw weld bead geometry.

[46] T Kannan and J Yoganandh. Effect of process parameters on clad bead geometry and its shape relationships of stainless steel claddings deposited by gmaw. *The International Journal of Advanced Manufacturing Technology*, 47(9):1083–1095, 2010.

[47] Shekhar Srivastava and RK Garg. Process parameter optimization of gas metal arc welding on is: 2062 mild steel using response surface methodology. *Journal of Manufacturing Processes*, 25:296–305, 2017.

[48] Raymond H Myers, Douglas C Montgomery, and Christine M Anderson-Cook. *Response surface methodology: process and product optimization using designed experiments.* John Wiley & Sons, 2016.

[49] Yudahira. H and Matsukawa. Y, 2007.

[50] Kawamoto. A Fujiwara. J, Mukai. Y and Kowa. M, 2011.

[51] InSoon Kim, K.J. Son, Yuansheng Yang, and P.K.D.V. Yaragada. Sensitivity analysis for process parameters in gma welding processes using a factorial design method. 43:763–769, 06 2003.

[52] Select Arc Welding Products. URL http://select-arc.com/products/pdf/welding_parameters.pdf.

[53] Robert E Kass, Uri T Eden, and Emery N Brown. Analysis of variance. In *Analysis of Neural Data*, pages 361–389. Springer, 2014.

[54] Gudmund R Iversen and Helmut Norpoth. Analysis of variance (no. 1). *Sage*, 1987.

[55] EWI. Gas metal arc welding basics: Welding current & welding voltage, . URL https://ewi.org/gas-metal-arc-welding-basics-welding-current-welding-voltage/.

[56] P Praveen, PKDV Yarlagadda, and Mun-Jin Kang. Advancements in pulse gas metal arc welding. *Journal of Materials Processing Technology*, 164:1113–1119, 2005.

[57] EWI. Gas metal arc welding basics: Travel speed and contact to work distance (ctwd), . URL https://ewi.org/gas-metal-arc-welding-basics-travel-speed-and-contact-to-work-distance-ctwd/.

[58] Marcel Hermans Gert Den Ouden. *Welding Technology.* 2009.

[59] Time temperature transformation diagrams, 2001.

[60] Kangda Hao, Chen Zhang, Xiaoyan Zeng, and Ming Gao. Effect of heat input on weld microstructure and toughness of laser-arc hybrid welding of martensitic stainless steel. *Journal of Materials Processing Technology*, 245:7–14, 2017.

[61] S. H. C. Park, Y. S. Sato, H. Kokawa, K. Okamoto, S. Hirano, and M. Inagaki. Microstructural characterisation of stir zone containing residual ferrite in friction stir welded 304 austenitic stainless steel. *Science and Technology of Welding and Joining*, 10(5):550–556, 2005. doi: 10.1179/174329305X46691. URL https://doi.org/10.1179/174329305X46691.

[62] Emel Taban, Eddy Deleu, Alfred Dhooge, and Erdinc Kaluc. Laser welding of modified 12toughness, microstructure and corrosion properties. *Materials & Design*, 30(4):1193 – 1200, 2009. ISSN 0261-3069. doi: https://doi.org/10.1016/j.matdes.2008.06.030. URL http://www.sciencedirect.com/science/article/pii/S0261306908002781.

[63] Erich Folkhard. *Metallurgical Phenomena in Secondary Crystallization of Stainless Steels and Weld Metals*, pages 78–102. Springer Vienna, Vienna, 1988. ISBN 978-3-7091-8965-8. doi: 10.1007/978-3-7091-8965-8_3. URL https://doi.org/10.1007/978-3-7091-8965-8_3.

[64] Pavel Krakhmalev, Ina Yadroitsava, G Fredriksson, and Igor Yadroitsev. Microstructure of slm manufactured 316l and 420 grades stainless steel. pages 59–66, 01 2014.

[65] Abdel-Monem El-Batahgy. Effect of laser welding parameters on fusion zone shape and solidification structure of austenitic stainless steels. *Materials Letters*, 32(2):155 – 163, 1997. ISSN 0167-577X. doi: https://doi.org/10.1016/S0167-577X(97)00023-2. URL http://www.sciencedirect.com/science/article/pii/S0167577X97000232.